Available online at www.sciencedirect.com

ScienceDirect

Underground Space 27 (2026) 150–174

www.keaipublishing.com/undsp

Research Paper

Investigation on jointed rock tunnel stability numerical database construction based on combined FDM–DEM approach

Rongmin Bai [a], Chuan He [a], Guowen Xu [a,*], Bo Wang [a], Xu Chen [a], Gaoyu Ma [a], You Zhou [a]

[a] *State Key Laboratory of Intelligent Geotechnics and Tunneling, Chengdu 610031, China*

Received 16 March 2025; received in revised form 18 June 2025; accepted 27 October 2025
Available online 05 January 2026

Abstract

Reliable data sources are essential for intelligent tunnel construction, yet on-site data are often insufficient to meet sample requirements. Previous numerical modeling studies have seldom considered the combined effects of different excavation methods' spatial effects and the distribution characteristics of joints. This paper develops a method to construct a stability database for jointed rock tunnels with primary support systems using a computational framework combining the finite difference method–discrete element method (FDM–DEM). The framework constructs a 2D model using the Mohr–Coulomb criterion and a 3D model with the Hoek–Brown failure criterion, enabling the stress release process to accurately replicate the influence of joint distribution features and excavation space effects in the 2D calculations by utilizing the longitudinal deformation profile parameters of the bench sections and fine-grained ground reaction curves. The computational circle is determined by grid research and data analysis, while the performance differences of various primary support components and their correlations with surrounding jointed rock are analyzed using the control variable method. The validity of the framework is initially confirmed by case comparisons and macroscopically validated using the Mantel test and Spearman analysis on the constructed simulation database—containing tunnel construction information, joint distribution, rock mechanics parameters, and stability indices—thereby establishing a reliable foundation for machine learning and transfer learning applications.

Keywords: Tunnel stability; Joint distribution; Stress release; Combined FDM–DEM; Database construction

1 Introduction

The rock mass is a highly non-linear and discontinuous medium, whose structural complexity and high anisotropy are compounded by the presence of non-continuous geological interfaces such as fractures, joints, fissures, and the random combination of jointed rock blocks (Li et al., 2021; Packulak et al., 2022). Analyzing the stress and displacement fields in the early stages of tunnel excavation in jointed rock is complex and must account for factors such as tunnel geometry, rock strength, excavation methods, and joint characteristics. This analysis is crucial for designing tunnel support systems and ensuring stability and safety (Zhang et al., 2023; Ma et al., 2023).

To handle this multifactorial problem, machine learning and multimodal models offer powerful tools to uncover hidden relationships (Wajid et al., 2023; Mou et al., 2023). Li et al. (2023) predicted carbon fiber performance using a convolutional neural network–multilayer perceptron hybrid model with visual and textual data. Chen et al. (2022) achieved strong results in seismic phase classification with the mask-to-feature–layout-to-image generation module. Liu et al. (2022) implemented asphalt pavement vehicle classification based on both time-domain and frequency-domain acoustic data using a deep transfer learning model. To dissect the implicit correlations between tunnel support systems and rock joint conditions, as well as excavation measures through multimodal learning, substantial and credible databases are needed, which

* Corresponding author.
E-mail address: xuguowen@swjtu.edu.cn (G. Xu).
Peer review under the responsibility of Tongji University

https://doi.org/10.1016/j.undsp.2025.10.002

should preferably include joint distribution maps, tunnel construction information, and corresponding stability indicators. While on-site testing offers the extent of damage in the affected area directly (Perras & Diederichs, 2016; Sun et al., 2021), it is too labor-intensive and time-consuming to be scaled up. Thus, numerical simulation becomes a practical alternative for integrating multi-source data in tunnel stability evaluation.

The discrete element method (DEM) is particularly effective for describing the mechanical behavior of discontinuous media like jointed rock mass in tunnel engineering (Sun, 2021; Bai et al., 2024), distinguishing rock matrix behavior from joints. Wang and Cai (2022) investigated the time-dependent deformations of a jointed rock tunnel with a creep model in 2D, while Fan et al. (2021) utilized advanced geological prediction to obtain the 3D discontinuous interface for tunnel stability analysis. However, 3D modeling faces greater complexity due to stereoscopic joint distributions, unlike simpler 2D models based on the 2D image of the practical excavation face. In contrast, 2D models cannot fully capture transverse stress redistribution and the longitudinal spatial effect caused by tunnel excavation, as illustrated in Fig. 1, which are fundamental factors affecting the mechanical response of surrounding rock and support structures (Feng et al., 2018; Bahrani et al., 2019). The convergence-confinement analysis method (Funatsu et al., 2008; Wang et al., 2024), which links longitudinal deformation profile (LDP) and ground reaction curve (GRC), simulates 3D effects through unloading processes. The GRC acquisition and the unloading process are typically derived via core replacement (Nie et al., 2018) or boundary stress release (Huang et al., 2017), as shown in Fig. 2. However, both methods often ignore the influence of excavation stages, joint distribution variability, and calculation control, which weaken the synergistic effect of excavation method and the joint distribution characteristic in 2D models.

To overcome these limitations and build a robust database for multimodal and transfer learning models, this paper proposes a simulation framework for analyzing the excavation and stability of jointed rock tunnels with primary support. The framework combines finite difference and discrete element methods, capturing the influence of joint geometry and excavation-induced spatial effects on tunnel behavior. Using the Hoek–Brown failure criterion, a 3D model is developed to derive LDP via the finite difference method (FDM), while DEM provides detailed GRCs through dense monitoring. Key parameters of the simulation cycle are identified through grid search and data analysis, and the control variable method is applied to explore the relationships between support performance, rock conditions, and excavation strategies. Finally, except for the results preliminarily validated through in-situ comparisons, the Spearman correlation analysis and the Mantel test are

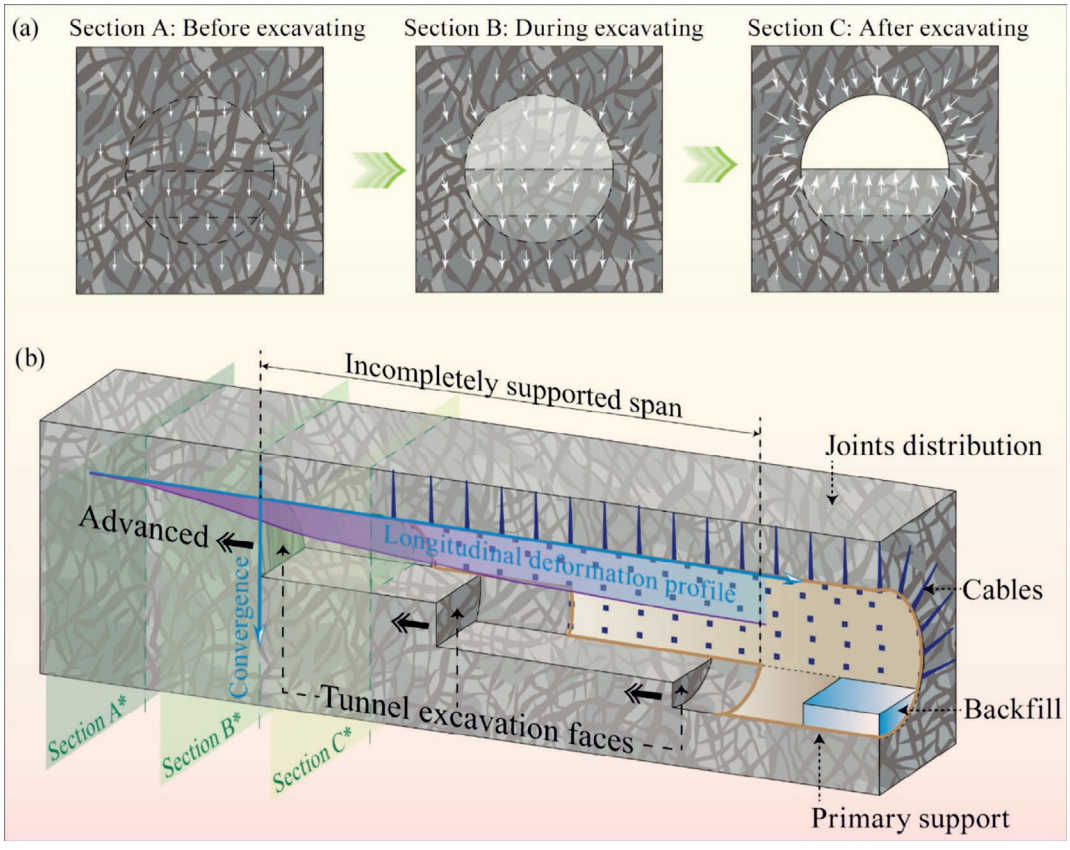

Fig. 1. Mechanical response of rock mass in tunneling. (a) Transverse stress redistribution, and (b) longitudinal spatial effect.

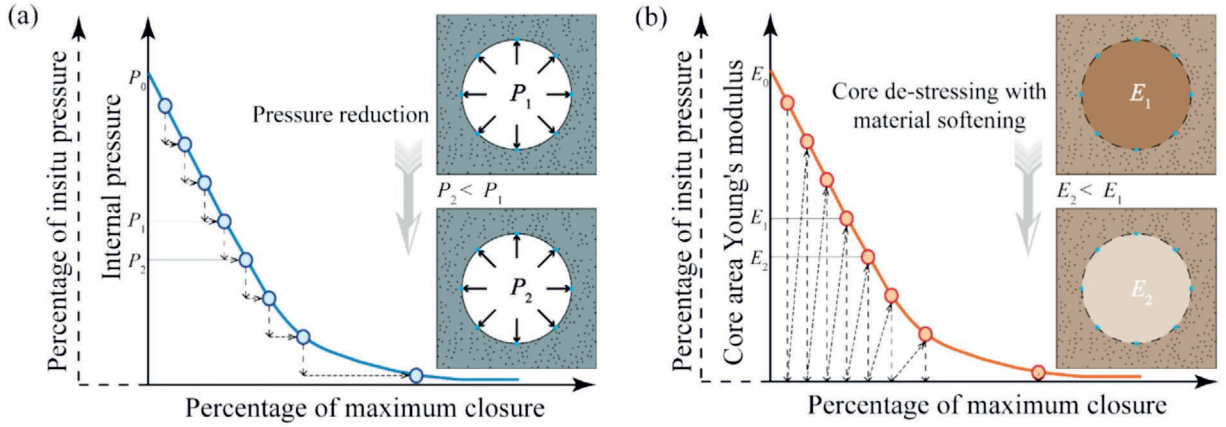

Fig. 2. Ground reaction curve acquisition method. (a) Boundary stress release, and (b) core replacement.

conducted to elucidate the relationship between diverse sources of tunnel information and tunnel stability, verifying the scientific validity and reliability of the constructed database from a big data perspective.

2 Theoretical and computational framework

To establish a numerical simulation database that optimally integrates and facilitates transfer learning with site data, this chapter applies the proposed computational framework and constitutive models using available joint geometry, lab-tested intact rock properties, and excavation and support data. For 3D models aimed at obtaining LDP, the Hoek–Brown (H–B) failure criterion is implemented in FLAC3D with FDM to integrate intact rock mechanical properties and joint characteristics. However, this homogenized method cannot capture joint plane weaknesses or slip behavior. To address this, the Coulomb slip model and Mohr–Coulomb (M–C) criterion are used in universal distinct element code (UDEC) with DEM to distinguish structural planes from the rock matrix and generate GRCs reflecting joint distributions. The exclusion of the slip model in 3D models, as mentioned earlier, is attributed to the increased complexity and diversity of 3D modeling compared to 2D data, as well as the greater challenges in acquiring such information in the field. Recognizing that numerical calculations involving multi-source heterogeneous data inevitably lead to inconsistencies, this chapter also explores the rational simplification of such contradictions.

2.1 Methodology for combined FDM–DEM applications

2.1.1 Application of the Mohr–Coulomb criterion in 2D models

Rock masses are typically sliced into numerous rock blocks by discrete joints; hence, in UDEC, rock masses are modeled as an assembly of bonded intact rock blocks ("Block") that interact at their boundaries, which are denoted as "Joint" (Stavrou & Murphy, 2018). Each block is subdivided into multiple zones ("Zone") and represented as a continuous deformable medium (Tan et al., 2020), as illustrated in Fig. 3. The inner deformation of each block discretized with triangles is given following an FDM calculation, and the outer blocks' interaction follows DEM principles.

The behavior of intact rock is modeled using the M–C criterion, with a failure envelope that incorporates a tension cut-off (Shen et al., 2020). The stress point position on the envelope is controlled by a non-associated flow rule for shear failure and an associated rule for tensile failure. As depicted in Fig. 3, if the calculated point falls outside the envelope, failure occurs: domain 1 indicates shear failure, domain 2 indicates tensile failure, both corrected through shear or tension plasticity.

The Coulomb slip model simulates slip and shear behavior at block contacts. As shown in Fig. 3, before shear failure, joint displacement follows linear deformation governed by shear and normal stiffness (Zhao et al., 2006; Chai et al., 2022). When shear force exceeds joint strength, failure occurs, leading to slip. At this stage, cohesion drops to zero, the friction angle remains constant, and joint behavior becomes fully friction-controlled.

The M–C model parameters are directly derived from intact rock tests. For joint cohesion and friction, polynomial fitting was applied using mechanical parameters of the surrounding rock and peak shear strength data from Chinese standard GB/T 50218—2014, yielding the curves in Fig. 4 with R^2 approaching 1. The joint stiffness parameters k_{jn} and k_{js}, are defined assuming an equivalent continuous deformable medium for the joint distribution state (Itasca, 2013) with Eq. (1):

$$\begin{cases} k_{jn} = \frac{E_m E_i}{s_j(E_i - E_m)} \\ k_{js} = \frac{G_m G_i}{s_j(G_i - G_m)} \end{cases}, \tag{1}$$

$$\begin{cases} c_j = 0.048c_m^3 - 0.123c_m^2 + 0.138c_m + 0.027 \\ \varphi_j = -0.001\varphi_m^3 + 0.099\varphi_m^2 - 3.705\varphi_m + 54.895 \end{cases}, \tag{2}$$

where E_m, E_i, G_m, G_i, c_j, φ_j, c_m, and φ_m are rock mass Young's modulus, intact rock Young's modulus, rock mass shear modulus, intact rock shear modulus, joint cohesion,

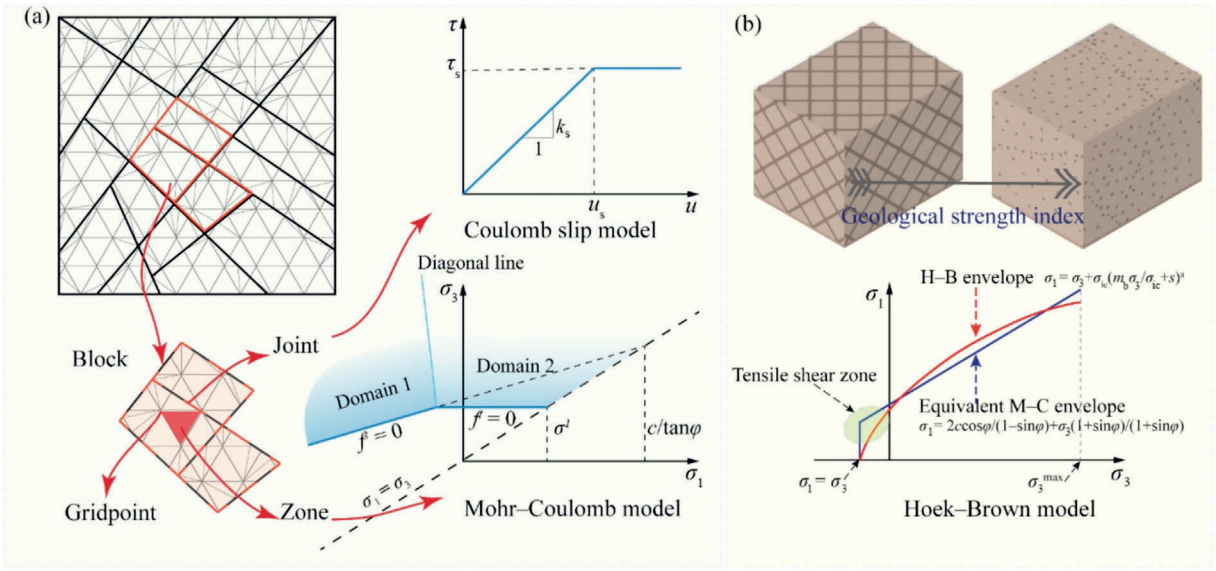

Fig. 3. Demonstration of 2D and 3D computational and constitutive models. (a) 2D jointed model, and (b) 3D homogeneous model.

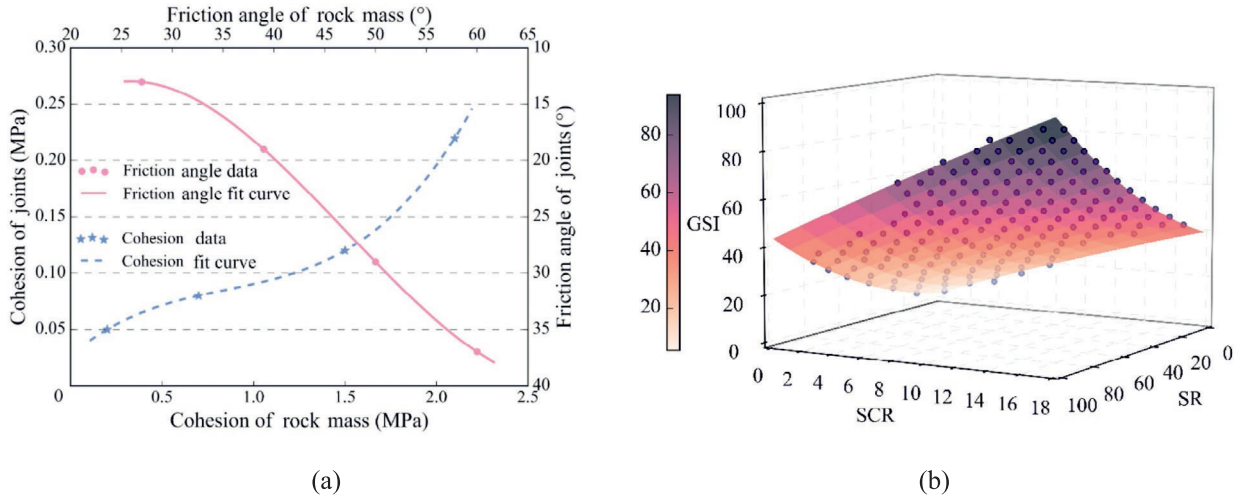

Fig. 4. Fitting results of model parameters. (a) Fitted curves of joint and rock cohesion and friction angle, and (b) GSI-SR-SCR polynomial mapped surface.

joint friction angle, rock mass cohesion, rock mass friction angle, the acquisition of rock mass mechanic parameters E_m, G_m, c_m, and φ_m will be mentioned in Section 2.1.3, and the expression for joint mean spacing s_j is as follows:

$$\begin{cases} s_j = \frac{n}{J_V} \\ J_V = N_1 + N_2 + \ldots + N_{n-1} + N_n \end{cases}, \tag{3}$$

where J_V is volumetric joint count, n is group of joints set, and N_n is the number of joints per unit length.

2.1.2 Utilization of the Hoek–Brown failure criterion in 3D modeling

Accurate 3D modeling of jointed rock masses requires accounting for joint spatial distribution, which remains technically challenging and often leads to modeling discrepancies and added complexity. Therefore, Hoek and Brown (1996) established the generalized H–B failure criterion based on non-linear Griffith theory, deriving an equivalent formulation from the M–C model, which is shown in Fig. 3. The H–B model incorporates joint effects into rock mass strength, establishing a quantitative link between lab-scale intact rock strength and engineering-scale parameters (Dai et al., 2024). It effectively captures the macroscopic mechanical behavior of jointed rock failure in 3D models.

Numerous scholars have obtained a series of Eqs. (2)–(4) through theoretical analysis and data verification, demonstrating the feasibility of obtaining mechanical parameters such as E_m, φ_m, and c_m from rock experimental data and geological strength index (GSI):

$$\begin{cases} E_m = E_i\left\{0.02 + \frac{1-\frac{D}{2}}{1+\exp[(60+15D-GSI)/11]}\right\} \\ \sigma_{mc} = \sigma_{ic}\frac{[m_b+4s-a(m_b-8s)]\left(\frac{m_b}{4}+s\right)^{a-1}}{2(1+a)(2+a)} \\ \varphi_m = \sin^{-1}\frac{3am_b(s+m_b\sigma_{3n})^{a-1}}{(1+a)(2+a)+3am_b(s+m_b\sigma_{3n})^{a-1}} \\ c_m = \frac{\sigma_{ic}[(1+2a)s+(1-a)m_b\sigma_{3n}](s+m_b\sigma_{3n})^{a-1}}{\sqrt{(1+a)(2+a)\{1+[6am_b(s+m_b\sigma_{3n})^{a-1}]\}}} \\ \sigma_{mt} = \frac{\sigma_{ic}}{0.81m_i+7} \end{cases}, \quad (4)$$

where σ_{mc}, σ_{ic}, and σ_{mt} are excavation disturbance parameters, rock mass compressive strength, intact rock compressive strength, and rock mass tensile strength, m_i is a material constant reflecting intact rock hardness, obtained via Hoek's method from laboratory tests; D represents excavation-induced disturbance, ranging from 0 (no damage) to 1 (severe disturbance), there exists the indirect strength of the rock mass σ_{3n}, the empirical parameters m_b, a, and s of rock measure one, can be calculated as

$$\begin{cases} \sigma_{3n} = \frac{0.47\sigma_m\left(\frac{\sigma_{mc}}{H\gamma}\right)^{-0.94}}{\sigma_i} \\ m_b = m_i exp\left(\frac{GSI-100}{28-14D}\right) \\ s = \exp\left(\frac{GSI-100}{9-3D}\right) \\ a = 0.5 + \frac{\left(e^{-\frac{GSI}{15}}-e^{-\frac{20}{3}}\right)}{6} \end{cases}, \quad (5)$$

where σ_m, H, and γ are rock mass compressive strength, tunnel depth, and density.

The GSI accounts for the impact of discontinuities and ranges from 5 to 100, with higher values indicating better rock mass quality. It depends on the interlocking condition between the structure rating (SR) and the surface condition rating (SCR). The SR is calculated by the joint volume density J_V in Eq. (6) while SCR sums the quality of roughness, weathering, and infilling.

$$SR = \begin{cases} 83.333 - 7.2382\ln(J_V) J_V \le 1 \\ 84.353 - 15.763\ln(J_V) 1 < J_V \le 60 \\ 30.005 - 3.2578\ln(J_V) 60 < J_V \end{cases}. \quad (6)$$

This study combines the guidelines provided by Sonmez et al. (2003) and Hoek and Brown (2019) with polynomial feature construction and linear regression model fitting methods to achieve the GSI fit with an R^2 value of 0.998, as depicted in Fig. 4.

$$\begin{aligned} GSI = {} & 2.3577 + 0.13608SR + 2.34628SCR \\ & + 0.00275SR^2 + 0.0109SR \times SCR \\ & - 0.015(SCR)^2. \end{aligned} \quad (7)$$

2.1.3 Support system element applications and assumptions

Besides the constitutive model settings, the simulation incorporates support structures. Tunnel primary support typically considers pre-grouting, rock bolt, steel arch, and shotcrete, modeled as "Cable" and "Liner" elements in UDEC.

Pre-grouting usually performed ahead of the excavation face, enhances surrounding rock stability via conduits and grout injection. Many researchers simulate its reinforcing effect as an equivalent reinforcement ring of certain thickness (Yasitli, 2013; Oke et al., 2014), as shown in Fig. 5. The homogenization principle is applied to average the conduit and grouting effect into the rock mechanical parameters (Zhao, 2015), leading to the following formula:

$$\begin{cases} \omega_{pg} = \frac{\pi d_{lc}^2}{4 s_{lcl} s_{lcc}} \\ c_{pg} = c_i + 0.6\omega_{pg}\sigma_{lc} \\ E_{pg} = E_i(1+\omega_{pg}) \end{cases}, \quad (8)$$

where s_{lcl}, s_{lcc} are longitudinal and circumferential spacing; d_{lc}, σ_{lc} denote diameter and tensile strength of the leading conduit; $\omega_{pg}, c_{pg}, E_{pg}$ represent effective enhancement rate, cohesion, and Young's modulus of the pre-grouting area; c_i is intact rock cohesion.

Bolts consolidation must account for both constraints across discontinuities and the inelastic deformation of intact rock in the failure zone around the excavation. Therefore, the cable element is used, enabling shear resistance along its length through interaction between the grout and surrounding medium, as shown in Fig. 5. Additionally, in tunnels experiencing large squeezing deformations, prestressed anchors are commonly employed to actively increase confining pressure. Numerically, this is modeled either by applying prestress directly or by enhancing surrounding material properties in this study, the modulus and cohesion of the zone around the cable are increased by 1.2 and 2 times, respectively (Yu et al., 2023).

Steel arches, typically combined with shotcrete, form a composite primary support structure. The Liner element includes an elastic–plastic material model that simulates the inelastic and ductile behavior of lining materials. It is suitable for generation along the domain boundary surface, making it ideal for representing primary support after excavation. Variations in arch spacing and thickness lead to differences in structural stiffness and density, so researchers apply the equivalent cross-section method, treating it as a homogeneous interface with equivalent mechanical properties (Carranza-Torres & Diederichs, 2009), from which the equivalent Young's modulus and density have been derived based on the shell theory of elasticity:

$$\begin{cases} E_{ps} = \frac{a_{sa}E_{sa} + t_{sc}s_{sa}E_{sc}}{a_{sa} + t_{sc}s_{sa}} \\ \rho_{ps} = \frac{a_{sa}\rho_{sa} + t_{sc}s_{sa}\rho_{sc}}{a_{sa} + t_{sc}s_{sa}} \end{cases}, \quad (9)$$

where E_{ps}, a_{sa}, E_{sa}, t_{sc}, s_{sa}, E_{sc}, $\rho_{ps,}$ and ρ_{sc} are the primary support effective Young's modulus, steel arch cross-section area, steel arch Young's modulus, sprayed concrete thickness, steel arch spacing, sprayed concrete Young's modulus, primary support effective density, and sprayed concrete density, respectively.

Additionally, the following assumptions are proposed or emphasized for the model calculations:

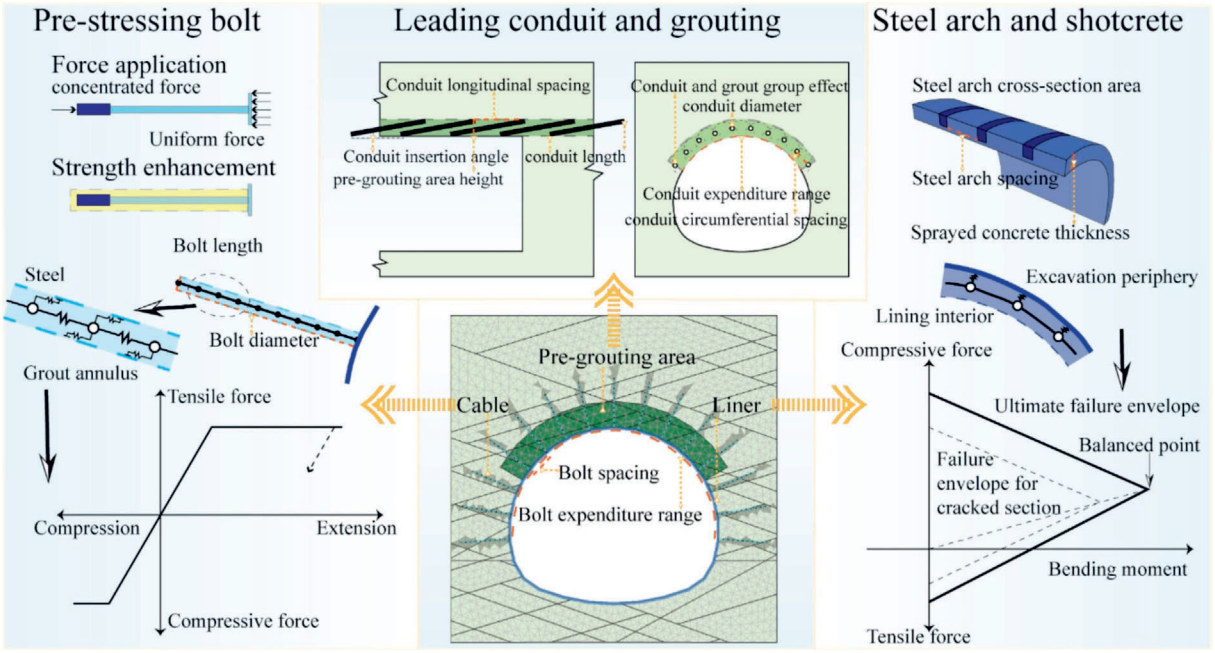

Fig. 5. Usage of 2D model primary support system in UDEC and interpretation of mechanical models.

(1) The mechanical parameters of the 3D model, derived from the joint distribution characteristics on the 2D tunnel face, assume that the LDP obtained within the interval is suitable for stress release processes in the 2D model with GRC;
(2) The boundary conditions involved in the 2D&3D models are defined by tunnel depth H and the lateral pressure coefficient k;
(3) As the simulation covers the complete construction sequence before the secondary lining, two specific values, T_{2D} and T_{3D}, represent the computation cycles per meter for the 2D&3D models, accounting for differing rock response times due to varying construction durations in reality.

2.2 Data generation framework and methodology

To construct a stability database for tunnel primary support systems considering the spatial effect of excavation and joint distribution characteristics, it is necessary to determine rock information, tunneling methods, and support system parameter ranges based on specific engineering backgrounds. Subsequently, Python is used to automatically generate UDEC and FLAC3D FISH files for iterative calculations across the following four modular processes, as shown in Fig. 6. Finally, the stability indexes are evaluated based on differences in the displacement and stress fields.

2.2.1 Construction of a random joint characteristic model

(1) A 2D model (80 m × 80 m) is generated using the "Joint" element in UDEC, where random joints are created based on their geometric parameters $[\theta_j^n, l_j^n, \rho_j^n]$ (dip angle, length and density of nth joint), as shown in Fig. 7.
(2) Tunnel excavation areas and benches are defined according to tunnel cavity geometry, primary support thickness, pre-reinforcement zones, and excavation method. This is saved as Model I.
(3) Integrate the tunnel span and height to create a unit mesh survey line, compute intersections with the joints, and determine the joint characteristic parameters $[J_V, s_j]$.

2.2.2 Acquisition of LDP for an unsupported system

(1) Calculate the SR based on the joint characteristic parameters of a cross-section calculated above. Obtain GSI through the fitting surface combined with SR and SCR as mentioned in Section 2.1.2, followed by rock mass parameters $[E_m, \varphi_m, c_m, \sigma_{mc}, \sigma_{mt}]$ derived from the intact rock and related parameters information $[\sigma_{3n}, m_b, s, a]$.
(2) To acquire LDP over different construction stages of the same section, rock mass information calculated are extended to an entire 3D model of 80 m × 80 m × 60 m combined with the H–B model as shown in Fig. 7. Segment the 3D model into excavation areas and mesh in accordance with construction details such as $[H_{ub}, H_{mb}, L_{ub}, L_{mb}, L_i, L_f, t_{sc}]$, where $H_{ub}, H_{mb}, L_{ub}, L_{mb}, L_i$, and L_f are the tunnel upper bench height, tunnel middle bench height, tunnel upper bench length, tunnel middle bench length, tunnel invert length, and tunnel footage, respectively. In case of full section excavation H_{ub}, H_{mb} are 0 and 2-bench excavation H_{mb} should be 0. To enhance sim-

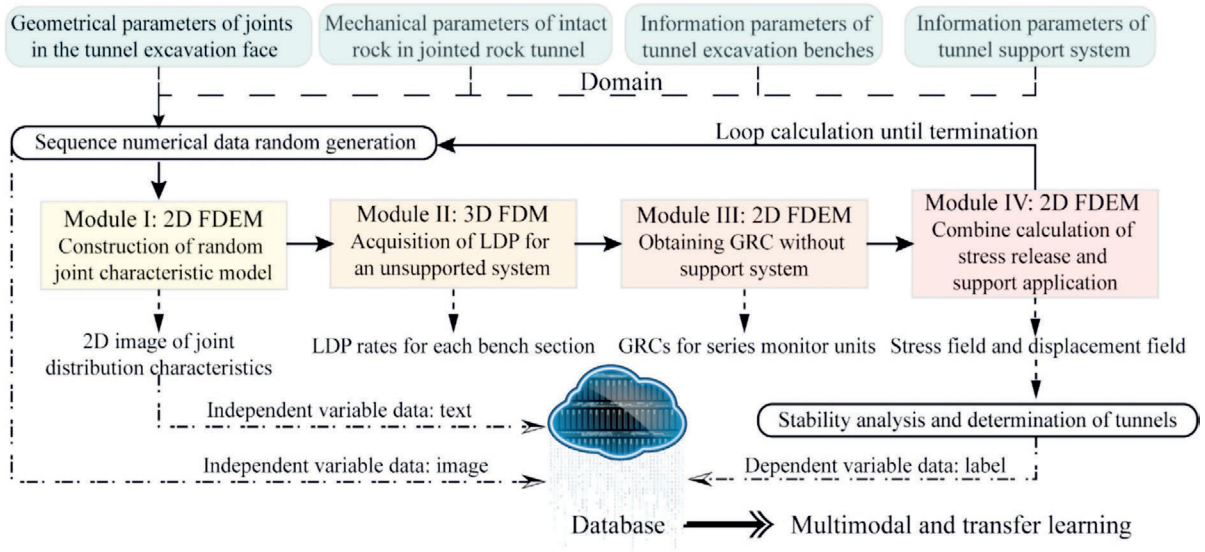

Fig. 6. Flowchart for constructing a database for combined FDM–DEM numerical simulation of tunnel stability.

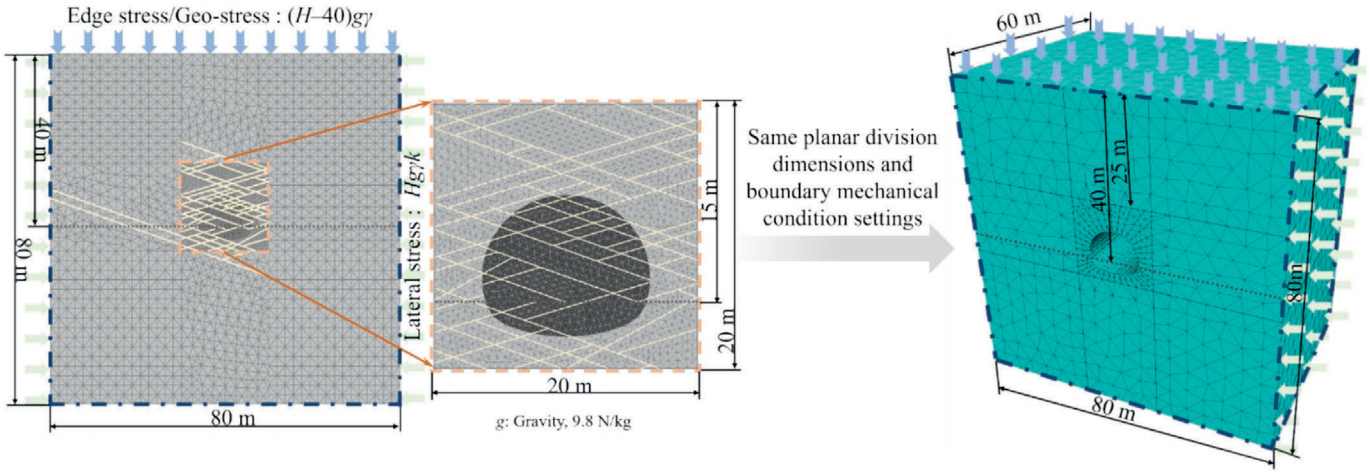

Fig. 7. Dimensioning, boundary condition presentation for 2D and 3D computational modeling cases.

ulation accuracy, a refined mesh is applied to the central 20 m × 20 m × 60 m region. Fixed boundary conditions (zero velocity) are imposed on all model faces except the top surface, indicated by dashed lines. A vertical load is applied on the top surface based on the burial depth and lateral pressure coefficient, while lateral stress fields are applied to the tunnel sides to simulate in-situ stress conditions.

(3) FLAC3D with FDM is conducted for tunnel excavation without initial support, where each bench excavation calculation circle is determined by the footage length and the T_{3D}. Additional circles are included post-excavation to capture delayed rock-support interactions. The total number of calculation cycles corresponds to the distance between the excavation face and the secondary lining application.

(4) Monitor the tunnel crown settlement as the radial convergence value, and combine it with the effective tunnel radius to derive the LDP. Depending on each cross-section bench length, obtain the corresponding convergence rate as a reference for subsequent stress release.

2.2.3 Obtaining GRC without support system

(1) Using the fitting curve introduced in Section 2.1.1, joint parameters $[k_{jn}, k_{js}, \varphi_j, c_j]$ are assigned based on rock mass properties. Assign the intact rock and joint parameters into the M–C model of the "Block" and the Coulomb-slip model of the "Joint" in Model I.

(2) Based on Model I, the mesh in the central 20 m × 20 m region is locally refined to improve accuracy while maintaining computational efficiency. As illustrated in Fig. 7, fixed boundary constraints (zero velocity) are applied along the dotted lines, and the initial stress field and longitudinal uniform load are defined according to tunnel depth and lateral pressure coefficient.
(3) Monitoring points are densely arranged around the tunnel boundary and benches to capture displacement ("Grid-point") and stress ("Zone") changes. Additional points are placed on the opposite side of the tunnel to simulate stress release and are saved in Model II.
(4) A core replacement method is applied to reduce deformation modules in 50 incremental steps during each excavation stage. This yields a set of GRCs for each monitoring point. For example, in a 2-bench excavation method, three sets of GRCs are generated: one for the weakened upper bench, one for the upper and lower benches combine weakened, and one for the entire weakened cross-section. Each set contains a unique number of GRCs.

2.2.4 Combine calculation of stress release and support system

(1) Pre-grouting areas in Model II are enhanced with corresponding parameters. Tunnel excavation is simulated according to the selected method, with stress release and support installation introduced after each stage. The calculation circles for these processes are determined by the current bench length and T_{2D}. Stress release calculations are also a period of unsupported and arch-erected post excavation process, considered as one steel arch spacing to reflect the engineering need to mitigate excavation face risks and stress redistribution in the surrounding rock.
(2) The stress release process involves applying stress and monitoring displacement at monitoring units based on the corresponding LDP parameters and GRCs. Specifically, as illustrated in Fig. 8, after boring the bottom bench in 2-bench excavation, initial stress release values for each monitoring point are determined from the corresponding GRCs and the LDP parameters of this cross-section. Apply stress to the corresponding unit's "Zone" and calculate once. These values are iteratively updated through repeated calculations, adjusting based on convergence data and adhering to the total cycle count established earlier. Potential issues with stress release rate continuity between different excavation stages are mitigated by the stepwise degree in GRCs, which will be further validated in the next section.
(3) Support elements ("Liner" and "Cable") are added to the newly excavated sections. The rock mass parameters in cable-anchored zones are also enhanced. The final calculation circles comply with the requirements specified in Module II, Step 3.
(4) Ultimately, deformation data from all monitoring points, as well as comprehensive displacement and stress field contours, are obtained for the entire model.

3 Model calibration and analysis

The calculation circles per meter for 2D&3D models critically influence LDP acquisition and the stress release process, and are directly linked to excavation length in the proposed computational framework. Given the limited research on calibrating this, this chapter determines the optimal T_{2D} and T_{3D} for unsupported tunnels using the grid analysis method and exhaustive mathematical analysis.

3.1 Engineering background

This study is based on the Chongqing–Kunming High-Speed Railway, which traverses three major geomorphic units: the low hilly red-bed basin, the plateau slope's middle mountains, and the high mountains of the Yunnan–Guizhou Plateau. The dominant rock types are basalt and sandstone, marked by strong tectonic activity and complex joint structures. The 700 km railway includes 81 tunnels, covering 49% of the total length, as shown in Fig. 9. Several tunnels with prominent joint distributions are classified as high-risk.

Based on pre-grouting design specifications, Table 1 summarizes parameters (θ_{lc}, l_{lc}, s_{lcl}, s_{lcl}, d_{lc}) and derives their equivalent values (h_{pg}, ω_{pg}) using Eqs. (2)–(8), where θ_{lc}, l_{lc}, s_{lcl}, s_{lcl}, h_{pg}, and ω_{pg} are the leading conduit insertion angle, leading conduit length, leading conduit circumferential spacing, leading conduit longitudinal spacing, pre-grouting area height, and pre-grouting effective enhancement rate, respectively. As the original data feature narrow and inconsistent intervals that hinder effective computation, they are discretized into uniform sequences as shown in Table 2. By incorporating excavation methods, geological reports, and support structure designs, Table 2 also defines the parameter range for database calculations. The variables σ_{it}, φ_i, μ, α_{lc}, l_b, s_b, α_b, and d_b represent the intact rock tensile strength, friction angle, Poisson's ratio, leading conduit expenditure range, bolt length, bolt spacing, bolt expenditure range, and bolt diameter, respectively. This range fluctuates around standard values and extends to boundary extremes, ensuring coverage of both routine conditions and high-risk scenarios. Notably, excavation methods are constrained: the bench length must be a multiple of the steel arch spacing, and in 2-bench and 3-bench

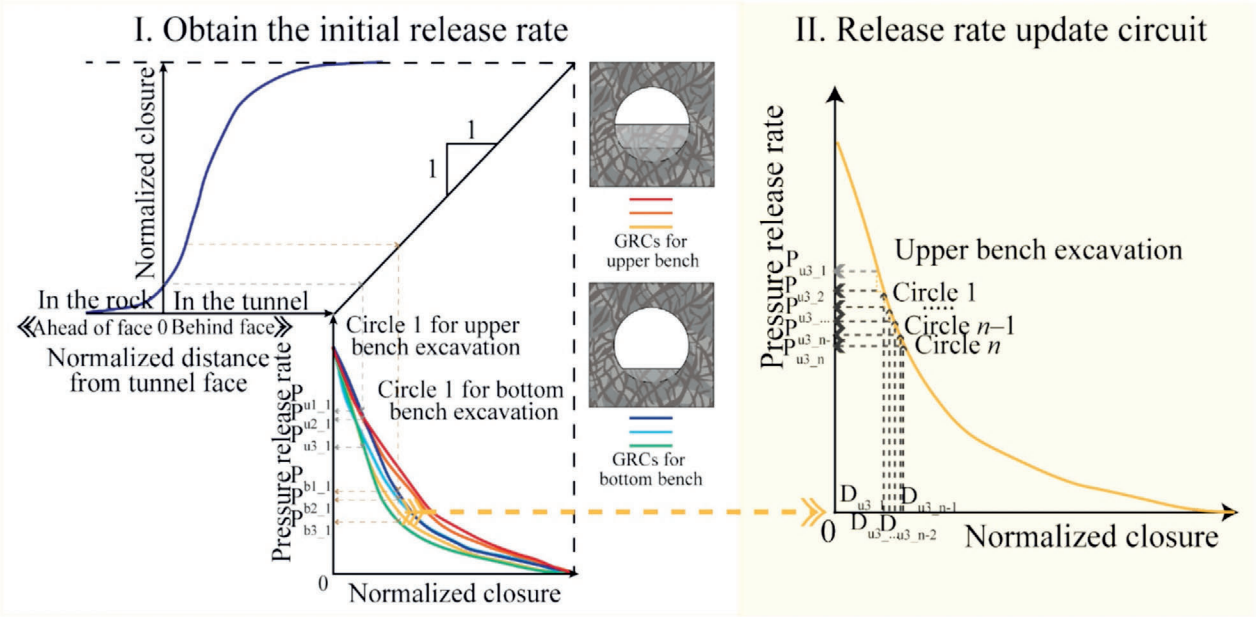

Fig. 8. Detailed implementation of stress release in combination with GRCs and LDP.

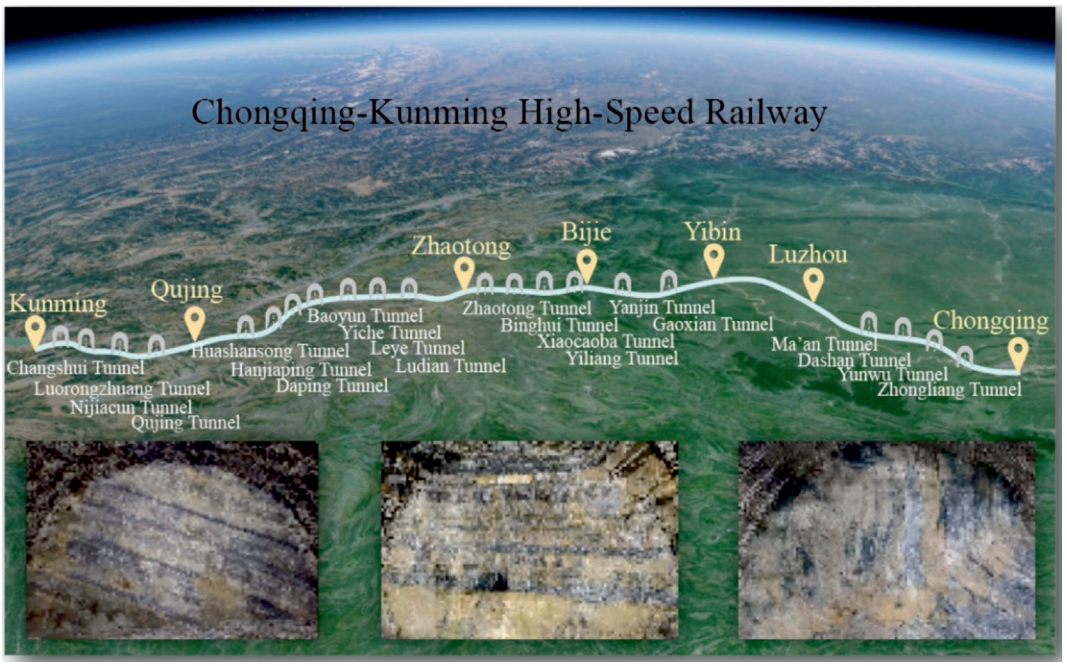

Fig. 9. Background of tunnel engineering with distinctive distribution of joints in the rock.

Table 1
Tunnel leading conduit support parameter and equivalent parameter conversion value.

Parameter	Unit	Large pipe roof	Middle pipe shed	Conduit
θ_{lc}	(°)	5	15	15
l_{lc}	m	35	9	4
s_{lcc}	m	0.4	0.4	0.5
s_{lcl}	m	30	(5.4,5.6,6)	(2.4,3)
d_{lc}	mm	108	(60,76,89)	42
h_{pg}	m	3	(1.56,2.32)	(0.69,0.88,1.0,1.3)
ω_{pg}	–	0.076	(0.115,0.117,0.126,0.203,0.278,0.288)	(0.115,0.92)

Table 2
Variable range of values for the tunnel multi-source heterogeneity parameter.

Information	Parameter	Range	Unit	Parameter	Range	Unit
Rock mechanical property	E_i	[10–100]	GPa	γ	[2000–2700]	kg·m^{-3}
	c_i	[2–30]	MPa	H	[200–1800]	m
	σ_{ic}	[25–150]	MPa	k	[0.5–2.5]	–
	σ_{it}	[1–20]	MPa	m_i	[3–30]	–
	φ_i	[20–60]	(°)	D	0.5	–
	μ	[0.2–0.4]	–			
Excavation method	H_{ub}	(3,4,5,6,7,8)	m	H_{mb}	(2,3,4)	m
	L_{ub}	[3–9]	m	L_{mb}	[3–9]	m
	L_i	[10–20]·s_{sa}	m	L_f	(2,3,4)·s_{sa}	m
Support system	α_{lc}	(90,120,150,180)	(°)	ω_{pg}	(0.1,0.2,0.3)	–
	h_{pg}	(0.7,1,1.3,1.6,1.9,2.2)	m	s_b	(1.2,1.5,1.8)	m
	l_b	(2.0,2.5,3.0,3.5,4.0,4.5)	m	α_b	200	(°)
	s_{sa}	(0.6,0.8,1.0,1.2,1.5)	m	d_b	24	mm
	a_{sa}	(0,I14,I16,I18,I20a)	cm^2	E_{sc}	(28,30,31.5)	GPa
	t_{sc}	(5,10,15,20,25,30)	cm			

Table 3
Tunneling multi-source information sequences for calibration analysis.

Parameter	E_i	c_i	σ_{ic}	σ_{it}	φ_i	μ	γ	H	k	H_{ub}	H_{mb}	L_{ub}	L_{mb}
Value	30	10	55	10	45	0.3	2300	540	0.95	6/4	0/3	4	4
Unit	GPa	MPa	MPa	MPa	(°)	–	kg·m^{-3}	m	–	m	m	m	m
Parameter	L_i	L_f	α_{lc}	h_{pg}	ω_{pg}	s_{sa}	a_{sa}	l_b	s_b	t_{sc}	E_{sc}	SCR	m_i
Value	10	2	120	1.6	0.2	1	26.13	3	1.5	20	28	13	10
Unit	m	m	(°)	m	–	m	cm^2	m	m	cm	GPa	–	–

configurations, upper bench height values are shown in italics and underlined, respectively.

3.2 Acquisition and calibration of LDP

Based on the computational framework in Section 2.2, a random tunnel face with three dominant joint sets was generated. Using fixed rock mechanics, support system, and tunneling parameters from Table 2, a representative dataset in Table 3 was created for LDP calibration experiments, GRC acquisition, and LDP-GRC calibration experiments.

To optimize the T_{3D}, simulations were conducted across a parameter grid: (50,100,150,200,250,300) × (All-section, 2-bench, 3-bench). The model calculations were performed for three different construction methods simultaneously to ensure that the optimal calculation circle accurately reflects the differences in the LDP curves caused by the different methods. As shown in Fig. 10, fifteen 3D models were computed, and Fig. 10(a)–(c) displays the impact of different circles on the LDP for the same construction method. As the cyclic parameter increases, the spatial effect of tunnel excavation shows a pattern of sudden intensification, gradual decline, and then another sharp increase. Notably, T_{3D} of 50 and 300 deviate significantly from the other cases. Since such anomalies are unlikely to result solely from changes in T_{3D}, and proper values should align with the linear trend observed during calibration, these two cases are excluded.

To further evaluate how different T_{3D} values influence the spatial excavation effects and normalized settlement (i.e., stress release rate) across tunnel cross-sections, a detailed multi-perspective analysis is presented in Fig. 11. As shown in Fig. 11(a), the stress release rate exhibits a pattern of rapid rise, stabilization, and subsequent sharp increase with increasing T_{3D}. Given the substantial impact of bench configuration on excavation-induced spatial effects, a representative T_{3D} should be selected to highlight differences between bench methods. Figure 11(b) illustrates the standard deviation of stress release rates across sections under the same construction method and T_{3D}, which also shows the aforementioned pattern, indicating 250 offers optimal sensitivity. Figure 11(c) further examines deviations within individual cross-section types, since the middle bench only exists in 3-bench construction, it is excluded. The upper bench shows sharp fluctuation between 50 and 150, stability thereafter, and another rise at 300. The bottom bench steadily declines until a slight increase at 300, while the invert section shows a consistent downward trend. These patterns indicate that $T_{3D} = 200$ or 250 best captures the excavation response with minimal noise.

Ultimately, 250 is identified as optimal T_{3D}. Figure 11(d) compares the LDPs of different excavation methods,

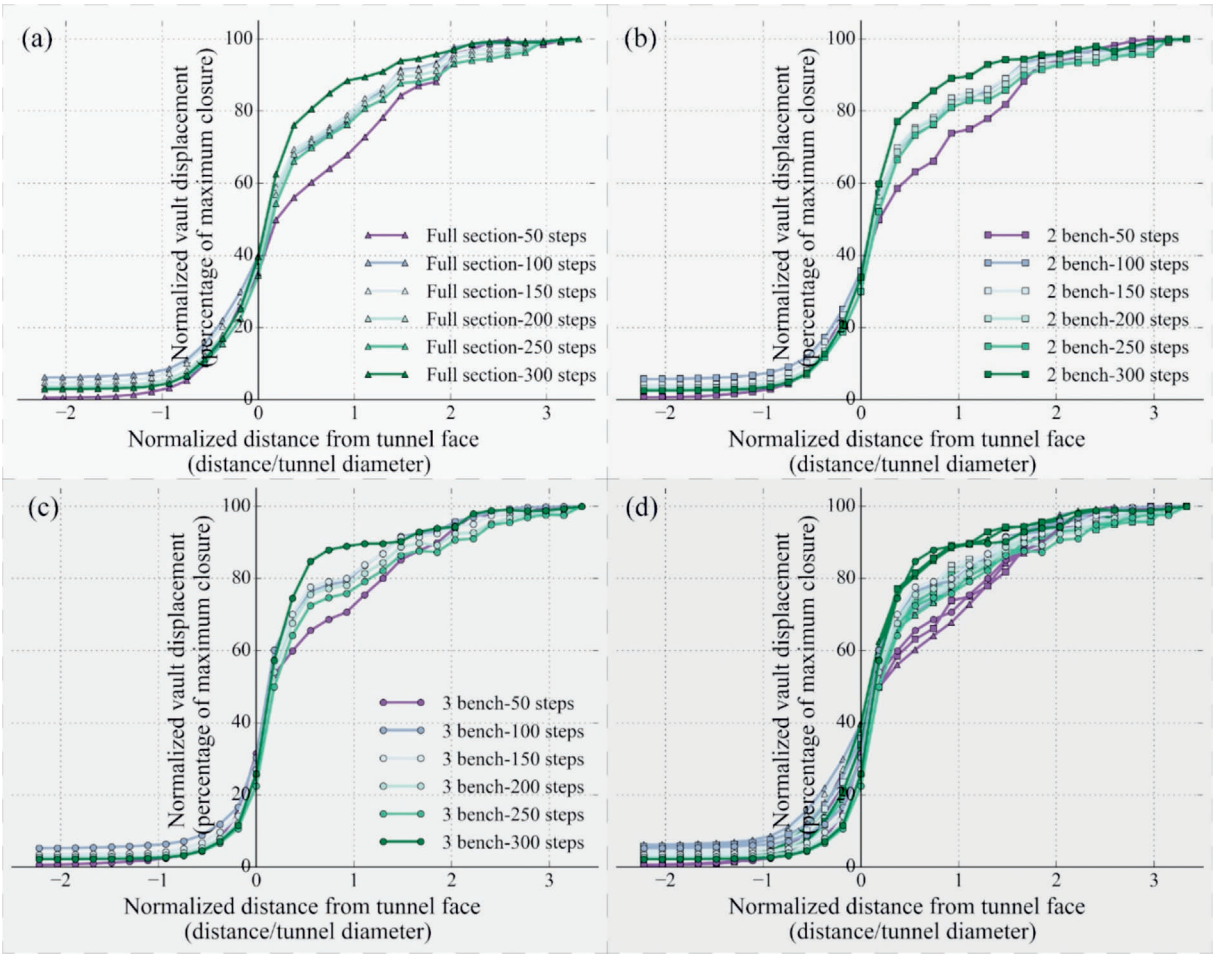

Fig. 10. Comparison of LDPs with different calculation circles. (a) LDPs for full section excavation method, (b) LDPs for 2-bench excavation method, (c) LDPs for 3-bench excavation method, and (d) LDPs among the three excavation methods.

revealing that increasing the number of benches reduces the disturbance at the tunnel face. Although the curves converge beyond 1/3 of the distance behind the face, differences in bench configuration still lead to distinct stress release responses across similar cross-sections.

3.3 Acquisition and variability of GRC

The GRC was derived from a randomly jointed cross-section (Fig. 12), indicating an interbedded gently dipping formation with variously sized wedge blocks near the excavation face. Simulations using different excavation methods yielded nine GRC series (Fig. 13). On average, these curves show a typical transition from elastic to plastic deformation during excavation.

However, detailed inspection of individual GRC subfigures reveals substantial variation across excavation methods, primarily due to stress redistribution induced by random joint patterns. Thus, when integrating LDP with GRC to determine stress release rate, it is essential to account for localized boundary effects rather than relying solely on averaged GRC values, which may obscure joint-related influences. Furthermore, the GRC in each subfigure is color-coded according to its relative position from the crown. An interesting phenomenon observed is that the blue curves generally lie above the red curves, indicating that the lower part of the excavation face in this type of gently dipping formation is less prone to entering the plastic deformation stage.

The impact of stress redistribution caused by different excavation methods is analyzed in Fig. 14, which centrally displays the average GRC for the nine cross-sections. As the bench number increases, the GRC gradient steepens, indicating that subdividing the excavation reduces the disturbance to the surrounding rock. Consistent with LDP analysis, GRC variations are pronounced at the upper bench but minimal at the invert. Therefore, Section 3.4 will analyze the overall effects of the combined LDP and GRC on the stress release process.

3.4 Implementation and calibration of stress release

The calibration method from Section 3.2 was similarly applied to assess stress release behavior under varying excavation strategies. A 6 × 6 parameter grid of T_{2D} = (50, 100, 150, 200, 250, 300) combined with (all-section,

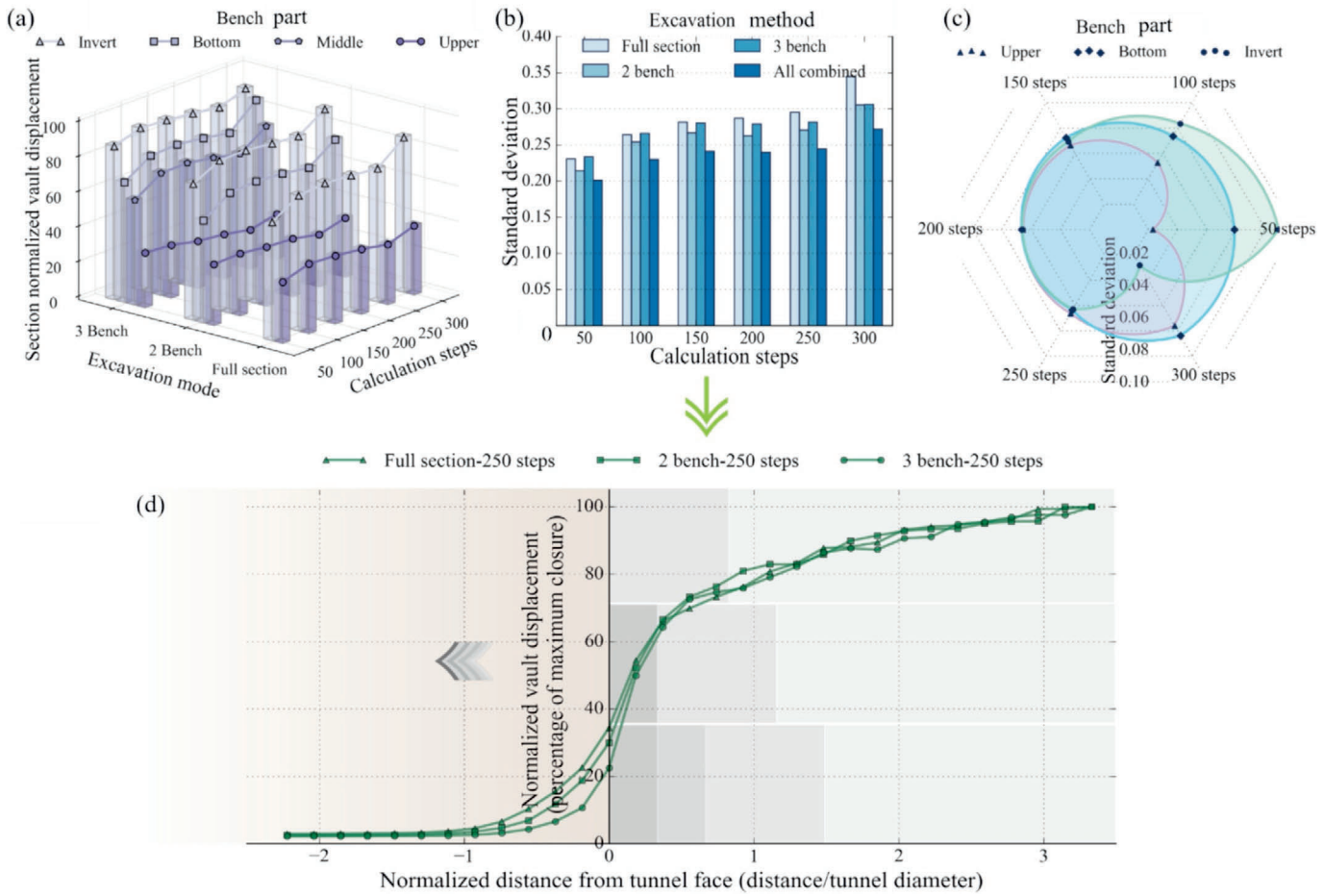

Fig. 11. Calculation circles optimal analysis for a series of LDP. (a) 3D displacement comparison across excavation methods under varying T_{3D} values, (b) standard deviation of displacement for different excavation methods at each T_{3D}, (c) radar plot of displacement standard deviation for various tunnel section types under different T_{3D}, and (d) LDP comparison of excavation methods under the optimal calculation circle.

2-bench, 3-bench) excavation modes and (stress release on/off) conditions yielded 30 simulation cases. As shown in Fig. 15(a), when stress release is disabled, tunnel deformation shows little sensitivity to T_{2D}, with nearly flat gradients. In contrast, enabling stress release significantly increases deformation with larger T_{2D}, especially beyond 150, highlighting distinctions between excavation methods. However, at T_{2D} = 200–300, deformation magnitudes become 2–5 times larger than those in the no-release case, making them unrealistic. Meanwhile, lower values (e.g., 50, 100) reduce deformations but fail to reflect differences among excavation modes. Therefore, 150 is identified as the optimal T_{2D}, balancing realism and method sensitivity.

Additionally, as previously mentioned, the stress release process should ideally reflect the disturbance differences caused by various excavation methods, and Fig. 15(b) further supports this conclusion. Without stress release, excavation method distinctions are poorly captured. When stress release is activated, the convergence optimization ratio between methods increases with T_{2D}, peaks at 150, then declines, reinforcing 150 as the ideal setting.

To interpret the unusual rise in deformation with larger T_{2D}, Fig. 16 visualizes displacement contours across excavation methods. Without stress release, deformation is concentrated at the crown and invert, with minimal excavation method differentiation. Upon enabling stress release, deformation shifts to the left haunch, arch foot, and invert, due to joint-induced sliding and extrusion in wedge-shaped blocks, especially on the left side. The crown, by contrast, remains relatively stable due to its funnel-like structure. Increasing the number of benches reduces deformation in these critical areas, indicating that multi-bench excavation better controls spatial disturbance.

The maximum and minimum principal stresses contour for the 2-stage excavation is shown in Fig. 17. Stress release relocates concentration zones from the crown and invert to sliding-prone blocks along the lower left and the wedge at the right arch waist, explaining why all methods show peak displacement at the left arch foot under stress release conditions. In summary, the stress release mechanism implemented in this study effectively replicates the spatial effects of tunnel excavation, accounting for excavation

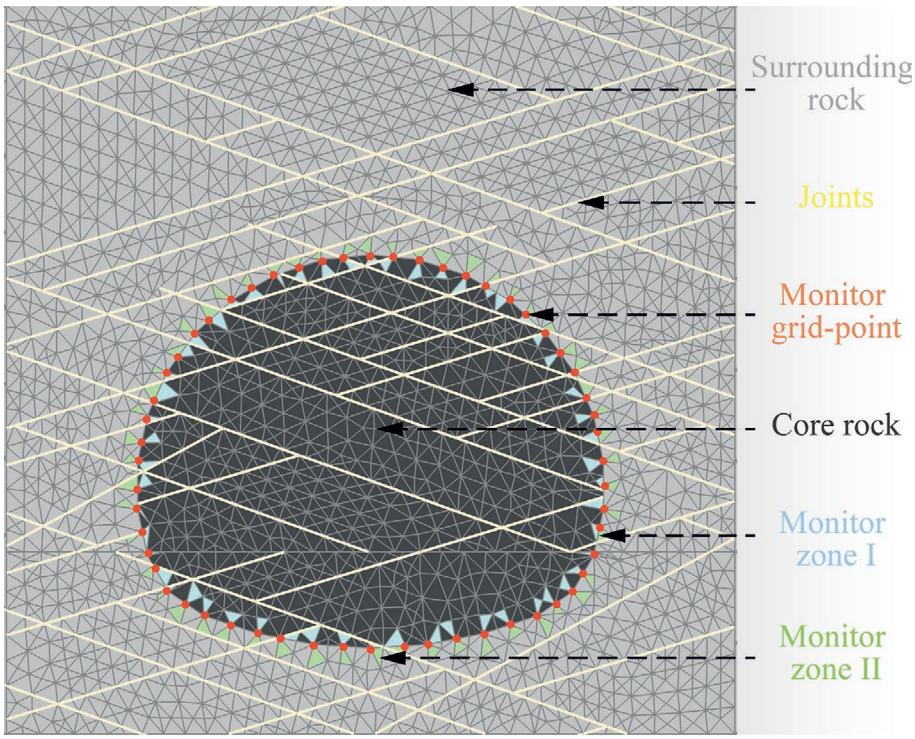

Fig. 12. Schematic of the 2D model with three sets of random joints.

sequence and the complex geometric distribution of joints, thus enhancing the model's realism and predictive capability.

4 Performance evaluation of the support structure system

To evaluate the impact of different support structures in the simulation, this chapter re-computes the tunnel models under optimal T_{3D} and T_{2D} using a control variable approach based on parameters from Section 3. Summary statistics of maximum tunnel deformation under single and combined structural effects are presented in Table 4. Multi-bench mode advantages remain evident, with primary support playing a significant role in deformation control, exceeding the effects of pre-grouting reinforcement and prestress bolt installation, which only have a minor impact. Subsequent sections analyze the individual and combined effects of support systems on tunnel stability, using a 2-bench case and integrating displacement, stress, and force field data. The effectiveness of the computational framework is also preliminarily validated through comparisons with field monitoring results and published studies.

4.1 Performance analysis under single factors

Tunnel deformation and maximum principal stress contour for single-support cases are displayed in Fig. 18. From the displacement field, pre-grouting effectively suppresses deformation near the vault but has limited influence on maximum deformation, especially in the left foot, previously identified as a key deformable zone. Similarly, bolts offer marginal control over maximum displacement.

From the stress field, the vault area, especially the joint contact block, shows an increase in the absolute value of the maximum principal stress, indicating an increase in compressive stress. This suggests that pre-reinforcement makes the surrounding rock in this area denser, enhancing its bearing capacity and stability.

Comparing the states before and after bolt application, there is a slight convergence in the deformation of joint contact surfaces around the tunnel, with relative convergence in the left haunch and foot. Due to the similar inclination angles of joints and bolt insertion angles in the left and right arch haunch, effective reinforcement is limited from the stress field, while only the vault exhibits improvement. Additionally, considering the force on the rock bolts themselves, significant axial force increases are noticeable at the stratum joints, as these areas are prone to sliding and compression deformations, making them relatively weak and causing the bolts to bear more load and play a reinforcing role.

The liner exerts the strongest influence on both stress and displacement. It constrains block movement around the tunnel, which in turn amplifies vault and invert deformations due to restricted motion and stress redistribution. The liner alleviates overall stress concentration, especially on the flanks, but shifts localized stress peaks—especially axial force—to the left foot area, aligning with wedge-shaped block behavior.

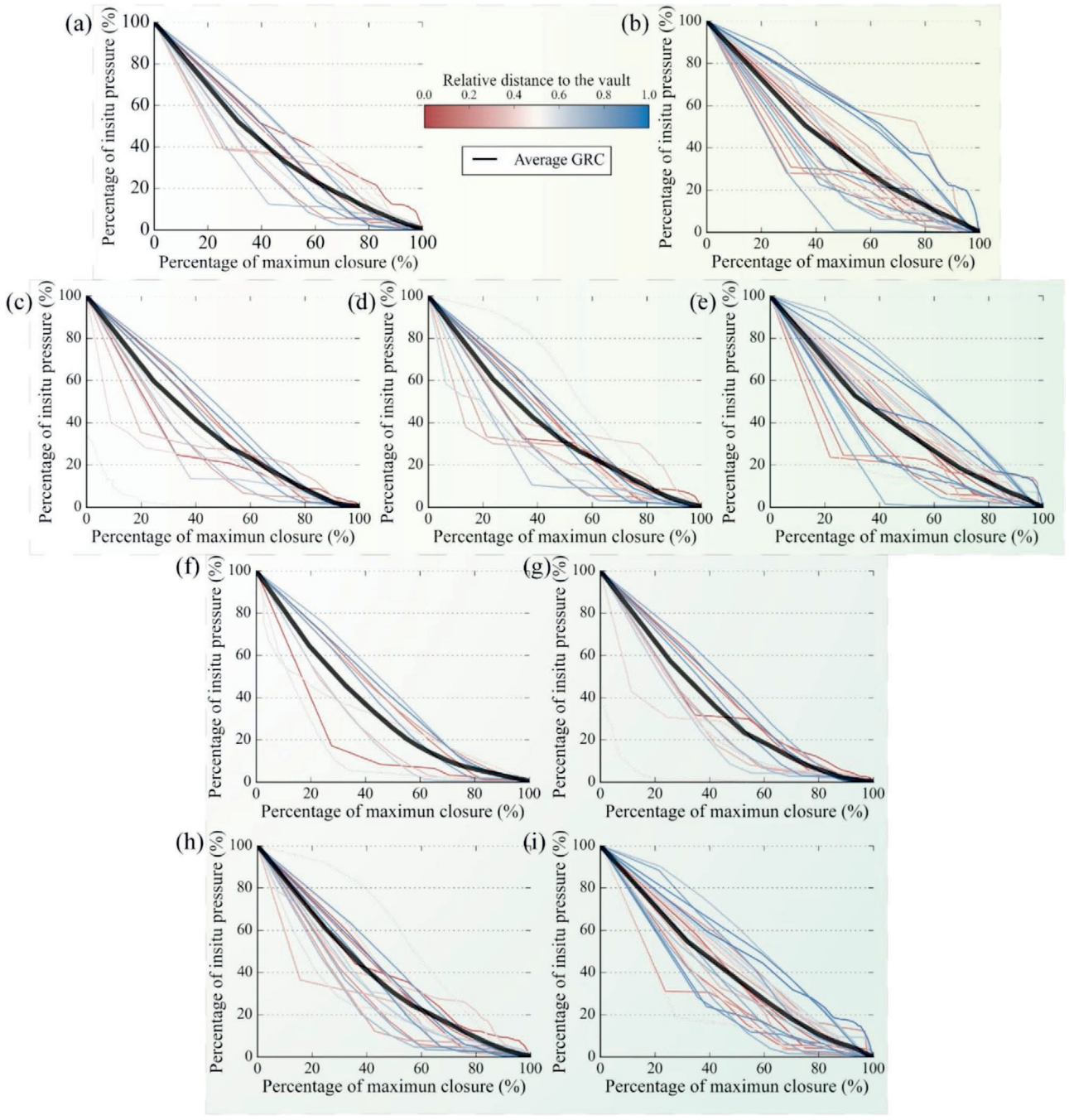

Fig. 13. GRC distributions for various excavation methods and tunnel sections. (a) Upper bench–full section method, (b) invert–full section method, (c) upper bench–2-bench method, (d) bottom bench–2-bench method, (e) invert–2-bench method, (f) upper bench–3-bench method, (g) middle bench–3-bench method, (h) bottom bench–3-bench method, and (i) invert–3-bench method.

In summary, pre-grouting reinforcement, prestress bolt installation, and liner application all contribute to tunnel stability in this developed program, with corresponding changes based on the distribution characteristics of joints.

4.2 Performance analysis under multiple factors

Tunnel deformation patterns across various support combinations are compared in Fig. 19. In a1 and a12, pre-grouting and bolts interact with the distribution of joints to help control tunnel displacement. Although their combined effect is limited, a slight convergence of the pink deformation limit region can still be observed at the left arch spandrel and arch haunch, as highlighted by the dashed circles in Fig. 19. The addition of a liner significantly improves displacement control. However, further reinforcement beyond the liner alone yields only marginal benefits, primarily seen as slight increases in axial force at the tunnel crown. In cases where both bolts and a liner are applied, initial stress concentrations at the liner's left

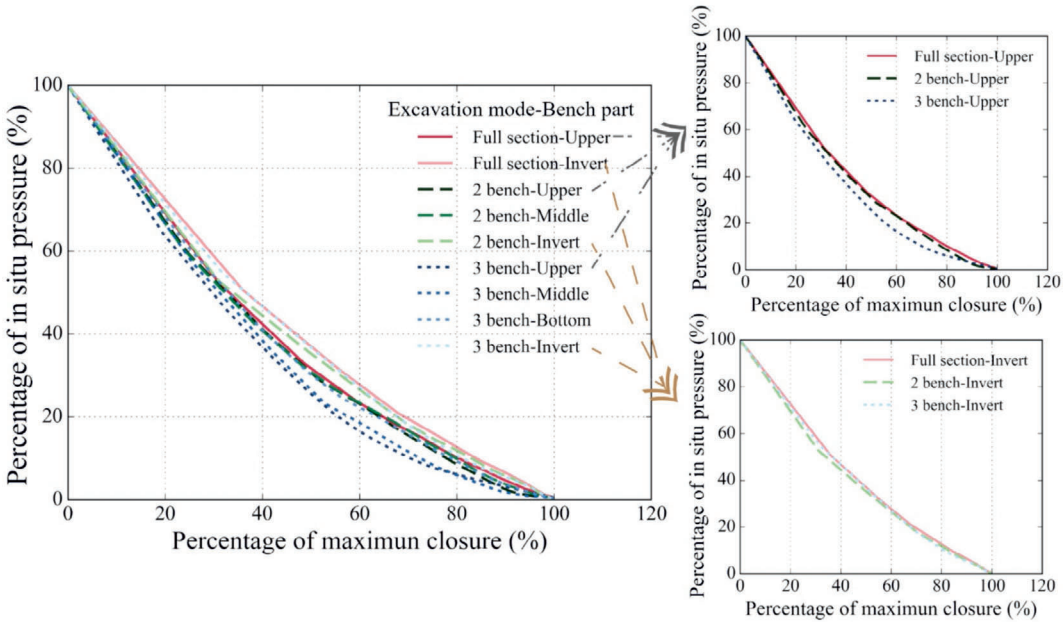

Fig. 14. Average GRCs for each excavation method and section of the tunnel.

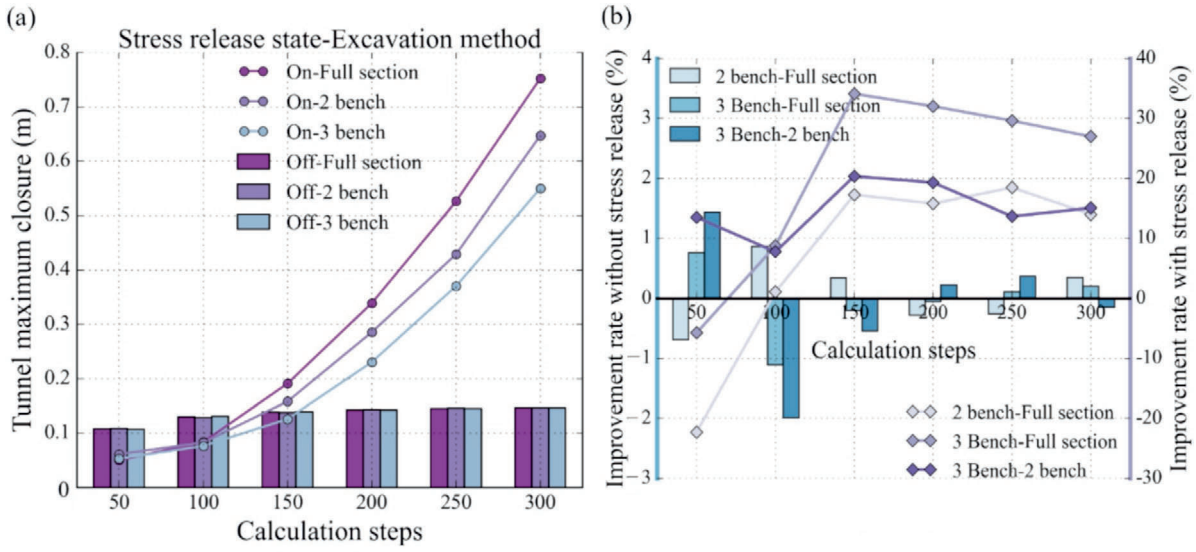

Fig. 15. Comparison of the impact of stress release on tunnel maximum deformation. (a) Differences in maximum deformation between excavation methods with and without stress release, considering various calculation circles, and (b) improvement ratios of maximum deformation across different excavation methods with and without stress release, considering various calculation circles.

footing become more evenly distributed. This indicates the bolts' role in coupling jointed rock blocks and redistributing loads, which helps reduce the risk of local cracking and enhances the overall structural integrity.

In conclusion, each support unit—pre-grouting, bolts, and liner—contributes uniquely to tunnel stability. Their combined application distributes loads more effectively and enhances tunnel performance under complex geological conditions, validating the effectiveness of the proposed simulation framework.

4.3 Computational framework engineering validation analysis

The Leye and Ludian tunnels were selected as case studies to validate the proposed computational framework, both being single-bore, double-track tunnels with spans of 14.86 m and heights of 12.54 m. The analysis focused on two specific sections: DK501+050 of the Leye tunnel and DK429+895 of the Ludian tunnel. These sections are geologically characterized by one dominant joint set with

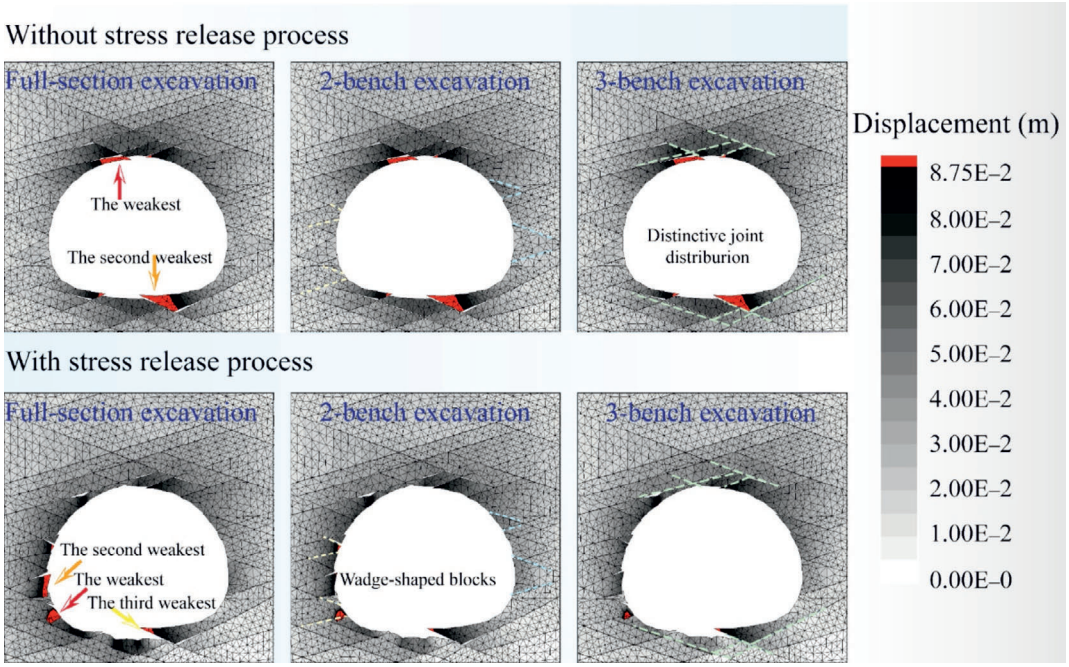

Fig. 16. Effect of stress release process on different excavation methods in the absence of support systems and considering joint distribution characteristics.

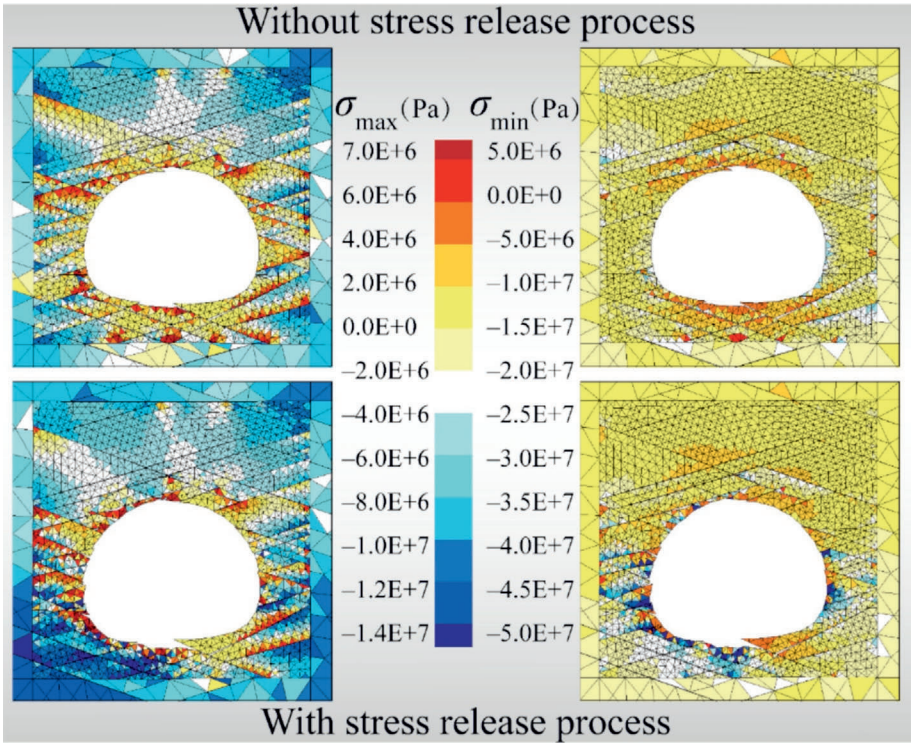

Fig. 17. Impact of the stress release process on the surrounding rock stress states at the optimal calculation circle using 2-bench excavation as an example.

a dip angle of 35°, intersected by two additional joint sets dipping at 40° and 100°, respectively, resulting in a complex rock mass structure. Due to the relatively weak and fragmented rock mass conditions in the Leye tunnel, a 3-bench excavation method was adopted to ensure stability and construction safety. In contrast, the more competent rock conditions in the Ludian tunnel allowed for the use of a 2-bench excavation approach. All relevant construction and geotechnical parameters used in the simulations—including rock mass properties, joint orientations, and excavation sequences—were obtained from Chen et al. (2025a, 2025b), as well as applicable design specifications and supporting laboratory test results. A comprehensive summary of these parameters is provided in Table 5.

Table 4
Summary of the maximum deformation of the tunnel by the same excavation method under the control variable method for the support system.

Support system			Maximum deformation of excavation method (mm)		
Area enhanced	Cable applied	Liner set-up	All-section mode	2-bench mode	3-bench mode
off	off	off	193.8	158.0	126.8
on	off	off	193.7	154.9	125.9
off	on	off	193.3	154.8	125.4
off	off	on	69.3	68.7	68.5
on	on	off	191.0	153.7	123.7
on	off	on	68.9	68.6	67.8
off	on	on	69.0	68.4	67.5
on	on	on	68.9	68.0	67.5

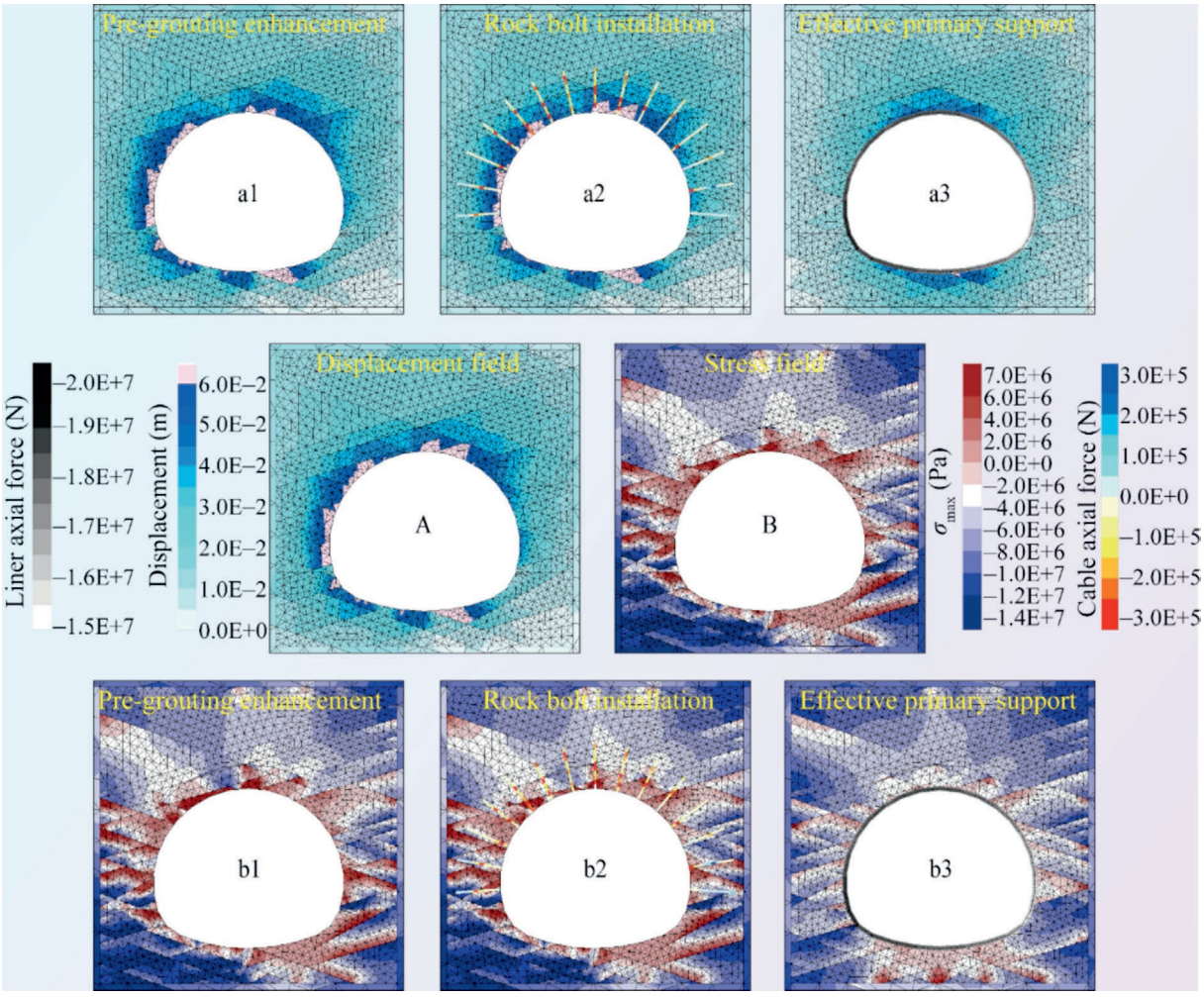

Fig. 18. Analysis of stress and displacement fields in tunnels considering the influence of individual support structure factors.

As illustrated in Fig. 20, the proposed computational framework integrates key joint characteristics—joint set count, dip angle, average density, and joint length—extracted from tunnel face imagery to generate a 2D jointed rock model for combined FDM–DEM analysis. Comparison of monitoring line and point displacements before the installation of the secondary lining—with and without applying the framework—demonstrates its ability to overcome limitations of traditional numerical models, particularly their tendency to oversimplify excavation-induced spatial effects and stress redistribution. This results in a significant reduction in the discrepancy between simulation outputs and field measurements. Further analysis of bar charts shows that in Case 1, monitoring point S2 exhibits greater deviation than S1, while in Case 2, S3 shows a notable improvement in accuracy. These differences are primarily attributed to joint sliding and wedge block extrusion, with the primary support system effectively buffering asso-

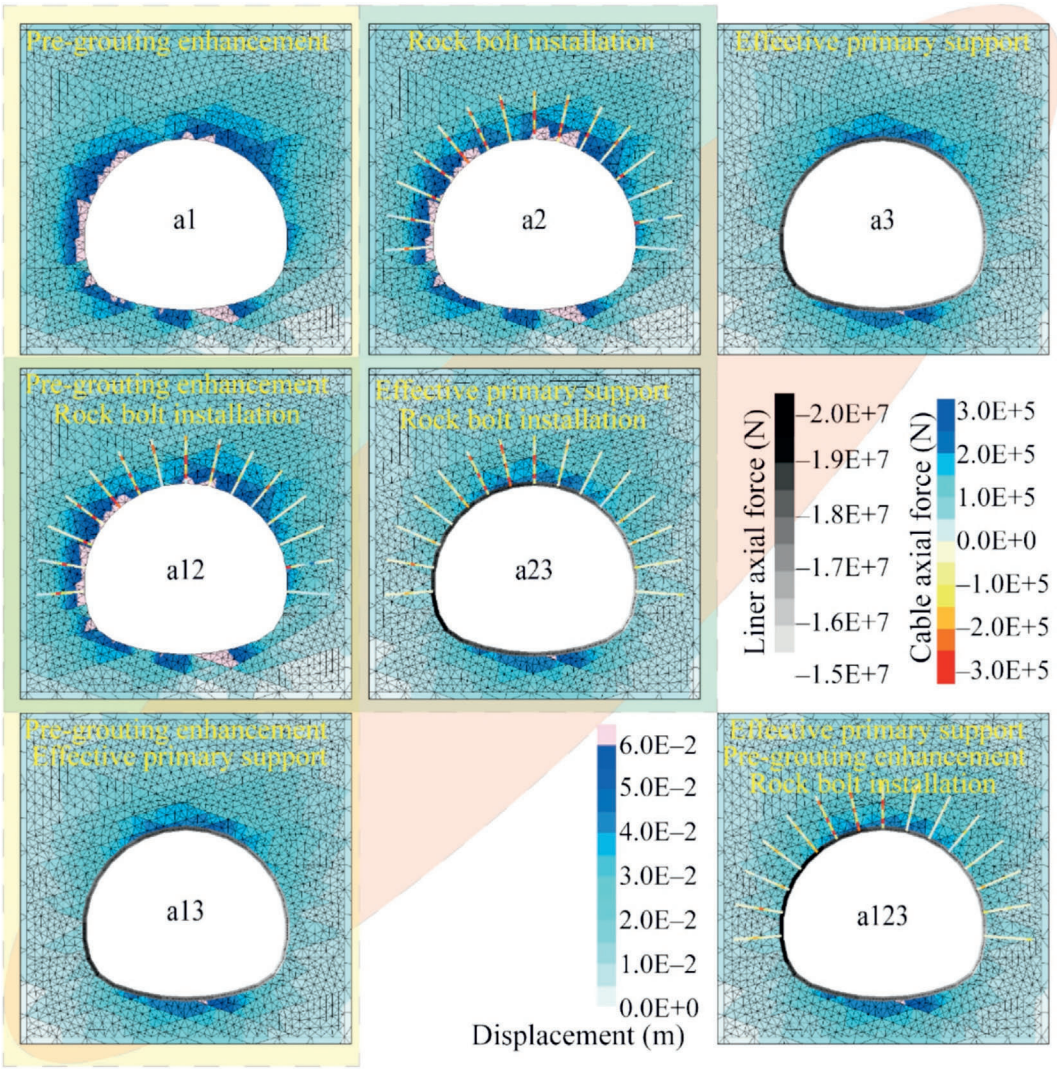

Fig. 19. Analysis of displacement fields and structural mechanics in tunnels considering the synergistic effects of multiple support structure factors.

Table 5
Specific parameters of the case tunnel.

Parameter	E_i	c_i	σ_{ic}	σ_{it}	φ_i	μ	γ	H	k	H_{ub}	H_{mb}	L_{ub}	L_{mb}
Leye	37	10.6	27.3	1.46	24	0.3	2655	263	0.95	3	4	4.8	6
Ludian	65	20.1	64.4	5.37	46	0.3	2578	390	1.05	6	0	8	0
Parameter	L_i	L_f	α_{lc}	h_{pg}	ω_{pg}	s_{sa}	a_{sa}	l_b	s_b	t_{sc}	E_{sc}	GSI	m_i
Leye	12	2.4	120	1.6	0.2	0.6	30.756	3.5	1.2	25	28	19.15	7
Ludian	16	3	120	1.6	0.2	1	26.131	3.5	1.2	25	28	20.86	8

ciated stress and deformation, confirming the framework's capability to capture the coupled behavior of jointed rock and support interactions.

To further validate the model, a case study at section DK429+895 of the Ludian tunnel was conducted, where additional instrumentation, bolt force, and rebar stress sensors were deployed to assess the relationship between joint distribution and support response. In Fig. 21(a), simulation results show overall agreement with measured values, though localized discrepancies persist in the arch-haunch regions, corresponding to zones with significant joint dislocation. Figure 21(b) highlights the framework's ability to replicate the transition from symmetric to asymmetric stress distributions, especially on the left side, consistent

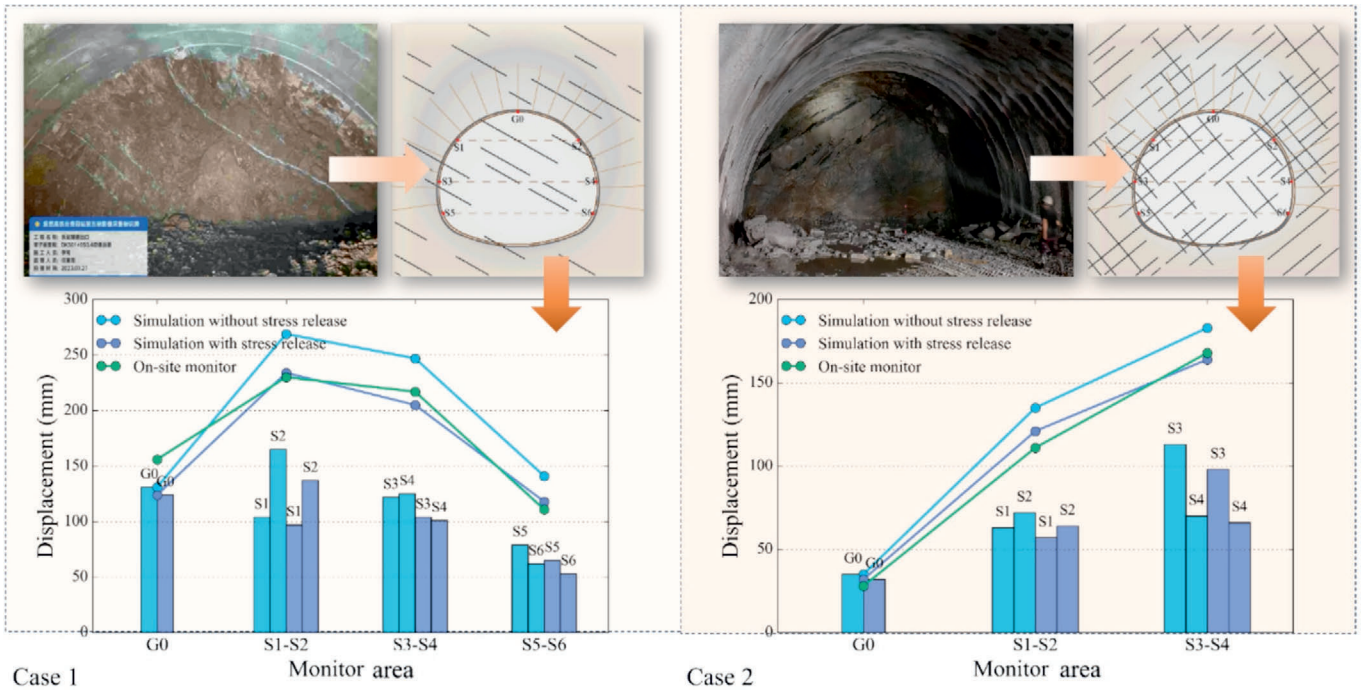

Fig. 20. Comparison between monitoring data of surrounding rock deformation and numerical simulation (Case 1: Leye Tunnel DK501+050; Case 2: Ludian Tunnel DK429+895).

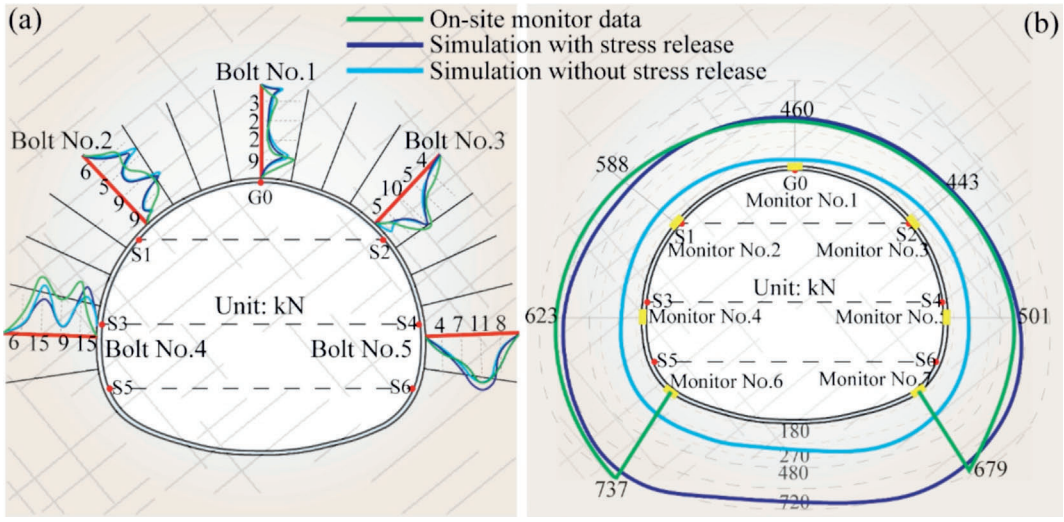

Fig. 21. Comparison of bolt and primary support mechanical monitoring data with numerical simulations.

with field observations. This shift is linked to stress redistribution and excavation-induced effects acting on wedge-shaped blocks and their interaction with support structures.

In summary, the proposed computational framework significantly improves the fidelity of tunnel excavation simulations by accurately modeling the complex interactions between jointed rock and support structures.

5 Database construction and macro-validation

Sections 3 and 4 confirmed that joint distribution characteristics and excavation-induced spatial effects can be effectively captured through combined FDM–DEM simulations, and that tunnel support performance is closely linked to the geometry of jointed surrounding rock. Building on this, the current chapter employs Python to automate the generation of random parameter sets and corresponding FISH scripts for FLAC3D and UDEC, enabling batch simulation of 1250 cases. Beyond previous case-by-case validation, this chapter applies big data analytics to the full dataset to evaluate the generalizability and practical alignment of the computational framework—laying a foundation for future multimodal and transfer learning applications.

5.1 Construction of stability indicators

To assess tunnel stability, a quantitative index is introduced based on whether the maximum displacement remains within design limits. Given the 13.3 m span and surrounding rock grades (III–V, mainly IV), the displacement threshold is set at 50 mm (NRA, 2017; Nguyen & Nguyen, 2015).

Data processing and analysis of the displacement results from various cases yield Fig. 22, showing that the tunnel's maximum displacement mainly falls within the 10–35 mm range, with a right-skewed distribution. Displacements exceeding 50 mm are considered warnings, with a safety-to-warning ratio of approximately 1:4.

Additionally, identifying zones of peak deformation is critical for timely support to prevent local instability and further deformation. Thus, the tunnel cross-section is divided into eight regions (Fig. 23), and the location of peak displacement is included for deep learning and multimodal training. Further statistical analysis of deformation regions in the database indicates that the tunnel haunch is most susceptible to severe deformation, followed by the vault and invert, while the arch foot remains comparatively stable. This distribution pattern closely matches field monitoring data, validating the model's capacity to reflect real-world behavior.

Analyzing the reasons for significant deformation in each part, for a single set of gently dipping joints, deformation typically concentrates at the vault or invert and shifts toward the arch shoulder as dip angle increases. In contrast, when multiple joint sets and wedge-shaped blocks are present, deformation localizes around the wedges, governed by their geometry and joint intersections.

5.2 Analysis and macro-validation of computational frameworks and database

Tunnel stability under randomly generated parameters and joint characteristics was assessed using three safety indicators: deformation status, convergence extremum, and deformity area. This section focuses on the first two indicators due to the high joint distribution characteristics dependency of deformity area, which limits its macro-level evaluation from text-based data.

To examine correlations between the support system, rock mass parameters, excavation methods, and safety indicators, both the Mantel test and Spearman correlation analysis were employed. The Mantel test evaluates the correlation between two distance matrices. In this study, high-dimensional discrete data (29 × 1250) representing system parameters were transformed using the Manhattan distance as Eq. (10), while lower-dimensional safety data (2 × 1250) were transformed using Euclidean distance as Eq. (11). Statistical significance of the Mantel correlation was determined through randomized permutation tests. Spearman analysis, a non-parametric method based on ranked values as Eq. (12), was used to assess monotonic

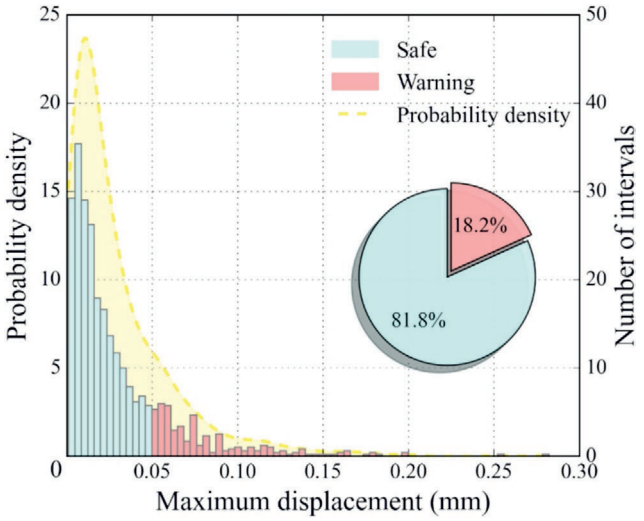

Fig. 22. Database scaled pie charts of safety states, maximum displacement distributions, and probability density diagrams.

relationships—particularly suitable for non-linear data such as convergence extremum with skewed distributions.

$$D_{\text{Manhattan}}(P,Q) = \sum_{i=1}^{n} |x_i - y_i|, \tag{10}$$

$$D_{\text{Euclidean}}(P,Q) = \sqrt{\sum_{i=1}^{n} (x_i - y_i)^2}, \tag{11}$$

$$P = \frac{\text{cov}[\text{rank}(X), \text{rank}(Y)]}{\sigma_{\text{rank}(X)} \sigma_{\text{rank}(Y)}}. \tag{12}$$

The results of Mantel's analysis and Spearman's analysis are presented together in Fig. 24, where Mantel's r portrays the statistical correlation. The larger the value, the greater the correlation. Usually, a value ≥ 0.5 is considered highly correlated, while a value <0.3 indicates a certain correlation. Mantel's p represents the significance of the correlation, with smaller values suggesting a rejection of the null hypothesis and indicating a significant correlation between the data sets. Given the multi-source heterogeneity of the factors in this experiment, a threshold of 0.1 for significance is set. Spearman parameters describe the nature and strength of the monotonic relationship between parameters.

From the analysis, most parameters exhibit significant or moderate correlations with deformation and convergence, except for middle bench parameters, pre-grouting height, and primary support strength parameters. The likely reasons are as follows: the middle bench applies only in 3-bench modes, reducing its statistical significance; pre-grouting height possibly meets requirements even at minimum height; primary support strength may have been homogenized via conversion to equivalent modulus by Eq. (8).

Spearman analysis indicates that rock geometrical and mechanical parameters, especially tunnel depth, Young's modulus, and cohesion, have the greatest impact on deformation status, followed by bench count and support type. The monotonic relationship between them is aligned with engineering understanding.

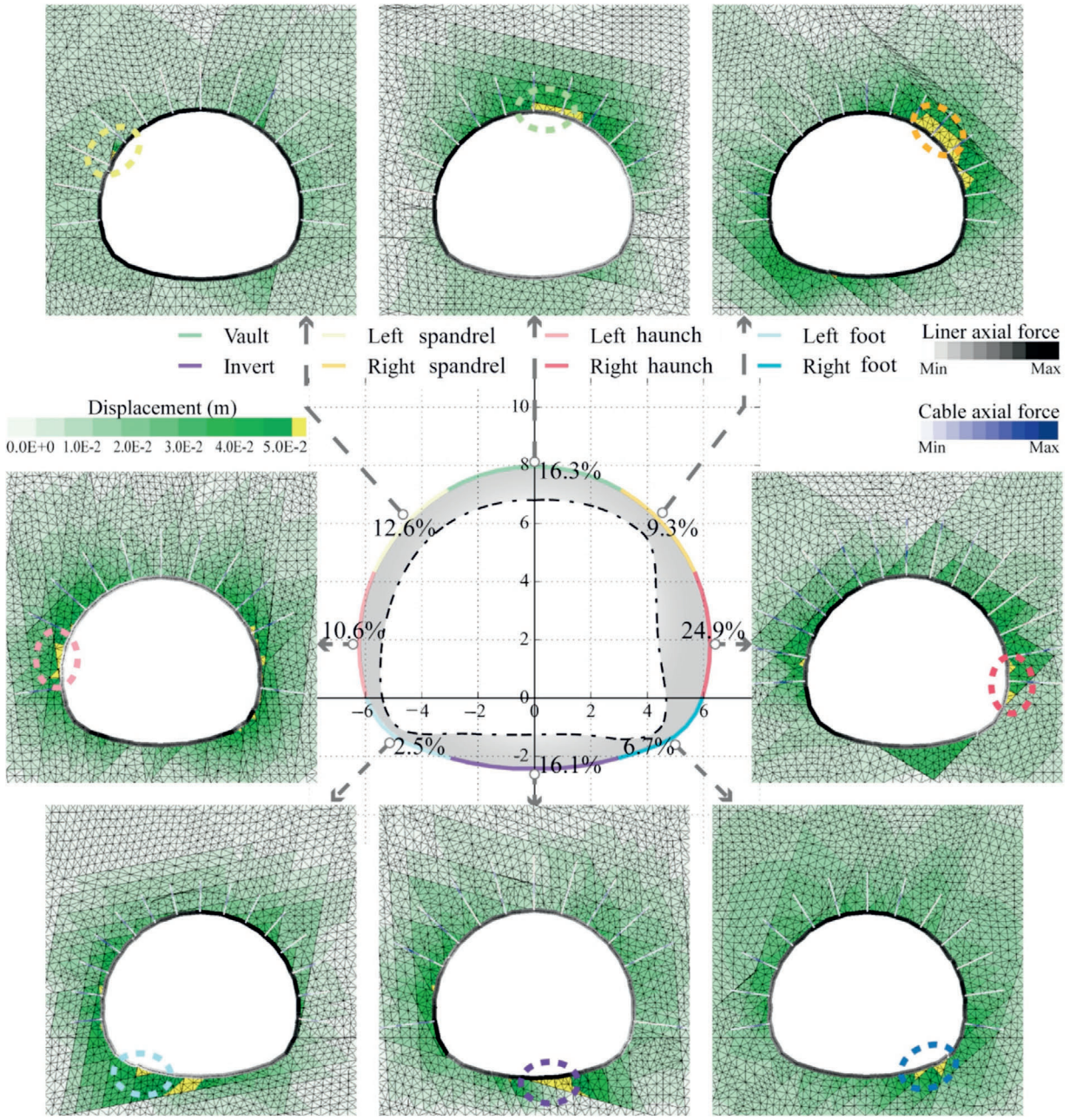

Fig. 23. Proportional distribution of deformation deformities in tunnel sub-areas under database and analysis of the contour map of surrounding rock and supporting systems with different conditions.

In summary, the database, constructed with consideration of joint distribution and excavation effects, accurately reflects real-world tunnel behavior. It offers a robust foundation for multimodal modeling and transfer learning, with its integrated numerical parameters, visual outputs, and safety indices grounded in both simulation rigor and engineering practice.

5.3 AI combined with database applications and foresight

The computational framework developed in this study integrates both joint image data and numerical data, covering rock geometric, mechanical properties, excavation techniques, and support systems relevant to tunnel construction. The artificial intelligence (AI)-driven application of this database is articulated through the approach and guidelines proposed in Fig. 25.

Both image data and numerical data are capable of individually predicting stability labels through methods such as ensemble learning and deep learning. However, it is worth noting that the image data may be primarily confined to predicting the deformity area, as joint patterns exhibit a strong correlation with this label. For enhanced predictive accuracy, both data types are fused via multimodal learn-

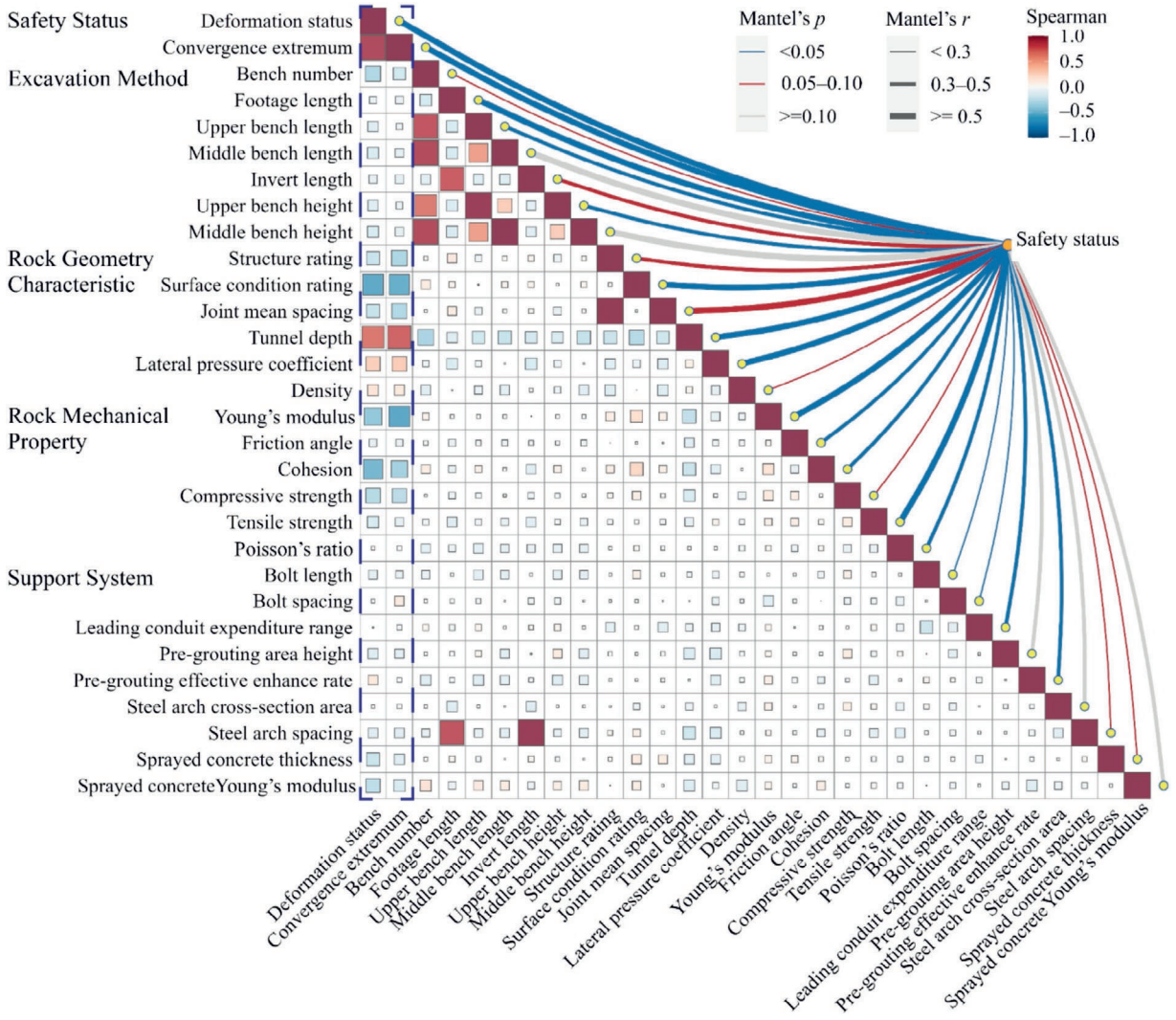

Fig. 24. Mantel test validation analysis and Spearman correlation analysis of tunnel safety status with support system, excavation method, and rock properties.

ing techniques that combine their complementary features. Furthermore, to enable practical deployment, semantic segmentation is employed to extract joint features from real tunnel face images, aligning them with the training dataset. Due to differences between field and training data, fine-tuning and transfer learning are required to adapt the model for robust performance in diverse engineering conditions.

6 Conclusions

This investigation has successfully developed and validated a computational framework for constructing a stability database containing numerical parameters, visual data, and stability indices for jointed rock tunnels using a combined finite difference-discrete element method. The key findings and contributions of this study are as follows:

(1) The developed computational framework combines the advantages of the M–C model in simulating jointed rock tunnel deformation and the Hoek–Brown failure criterion in homogenizing jointed rock on the excavation longitudinal scale to obtain the deformation profile, while also effectively restoring stress release, particularly simulating the extrusion and slip phenomena of the rock mass blocks formed by interlocking joints, as well as capturing the influence of joint distribution features and excavation space effects.

(2) Through grid analysis and case comparisons, the optimal computational circle number per meter for both 2D and 3D models was determined. This ensures accurate replication of the stress release process and the influence of joint distribution features during tunnel excavation.

(3) The study evaluated the performance of key support elements for jointed surrounding rock, including pre-grouting, bolts, steel arches, and shotcrete. Results validated that the multi-stage excavation method was particularly effective in controlling deformation.

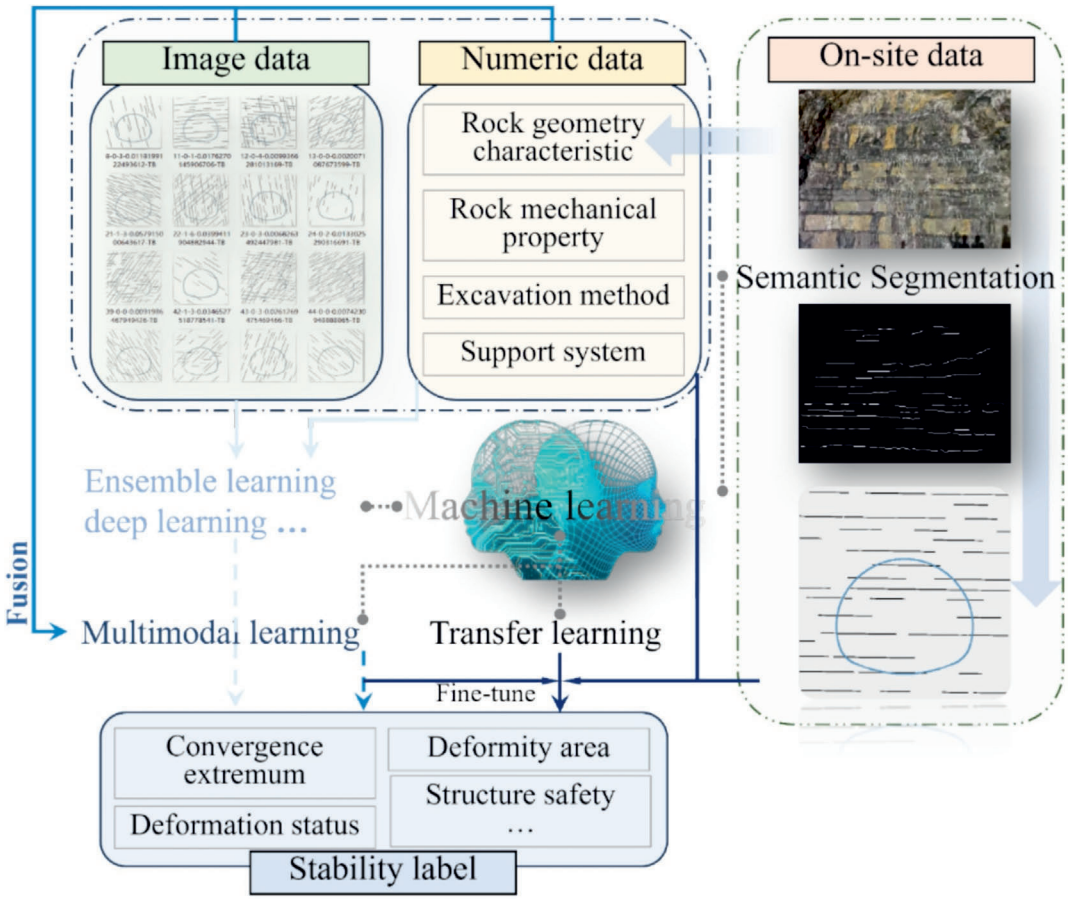

Fig. 25. Schematic flow of AI-enabled applications relying on the combined FDM–DEM computational framework.

The primary support system demonstrated the highest effectiveness, significantly outperforming pre-grouting and bolts, while bolts contributed specifically to deformation control at the jointed surface.

(4) Mantel test and Spearman correlation analysis were employed to explain the relationships between the support system, rock parameters, excavation mode, and safety indicators. The results indicated that rock geometry and mechanical parameters, particularly tunnel depth, Young's modulus, and cohesion, had the greatest impact on deformation status. The number of excavation benches and primary support parameters also significantly influenced tunnel stability.

(5) The database was constructed to include information on the joint distribution of excavation face, tunnel rock parameters, construction parameters, and stability indexes. Big data analysis techniques were employed to validate the database on a macro-scale, confirming its consistency with real-world tunneling conditions and supporting its use in machine learning and transfer learning applications.

Data availability

The data that support the findings of this study are available from the corresponding author upon reasonable request.

CRediT authorship contribution statement

Rongmin Bai: Writing – original draft, Methodology, Investigation, Conceptualization. **Chuan He:** Writing – review & editing, Supervision, Project administration, Funding acquisition. **Guowen Xu:** Writing – review & editing, Supervision, Methodology, Funding acquisition, Conceptualization. **Bo Wang:** Writing – review & editing, Supervision, Project administration. **Xu Chen:** Validation, Methodology, Investigation. **Gaoyu Ma:** Validation, Investigation. **You Zhou:** Validation, Investigation.

Declaration of competing interest

The authors declare that they have no known competing financial interests or personal relationships that could have appeared to influence the work reported in this paper.

Acknowledgement

This research was supported by the Natural Science Foundation of China (Grant No. 52378416), the Research and Development Program of China State Railway Group Co., Ltd. (Grant No. N2024G050), and the Science and Technology Department of Sichuan province (Grant No. 2024YFCY0017).

References

Bahrani, N., Valley, B., & Kaiser, P. K. (2019). Influence of stress path on stress memory and stress fracturing in brittle rocks. *Canadian Geotechnical Journal, 56*, 852–867.

Bai, R. M., He, C., Xu, G. W., Wang, S., & Shu, Y. H. (2024). Investigation of Phyllite-based Brazilian tests and fracture failure patterns via AE and PFC3D. *Bulletin of Engineering Geology and the Environment, 83*, 113.

Carranza-Torres, C., & Diederichs, M. (2009). Mechanical analysis of circular liners with particular reference to composite supports. For example, liners consisting of shotcrete and steel sets. *Tunnelling and Underground Space Technology, 24*(5), 506–532.

Chai, S. B., Zhou, T., Tian, W., Jing, Y. L., & Shi, J. H. (2022). Analysis of stress wave propagation through a rock structural plane considering rock mass stresses. *Rock and Soil Mechanics, 43*(S1), 184–192 (in Chinese).

Chen, X., He, C., Xu, G. W., Bai, R. M., Yuan, Q. Y., & Ma, G. Y. (2025a). Analytical solutions for deep tunnels in viscoelastic-plastic rock considering rheological damage effects and the lining influence. *Rock Mechanics and Rock Engineering, 58*, 1117–1145.

Chen, X., He, C., Xu, G. W., Wang, B., Ma, G. Y., & Du, J. M. (2025b). Stabilisation time analysis method for deep tunnels considering rheological effects and lining influence. *Tunnelling and Underground Space Technology, 155*, 106170.

Chen, X. Y., Zou, Q., Xu, X. X., & Wang, N. (2022). A stronger baseline for seismic facies classification with less data. *IEEE Transactions on Geoscience and Remote Sensing, 60*, 1–10.

Dai, J. H., Gong, F. Q., He, Z. C., & Xu, L. (2024). Quantitative estimation method for the excavation-induced weakening effect of rock mass parameters in deep tunnels. *Engineering Geology, 330*, 107416.

Fan, H. Y., Li, L. P., Liu, H. L., Shi, S. S., Hu, J., & Zhou, S. (2021). Advanced stability analysis of the tunnels in jointed rock mass based on TSP and DEM. *KSCE Journal of Civil Engineering, 25*(4), 1491–1503.

Feng, X. T., Xu, H., Qiu, S. L., Li, S. J., Yang, C. X., Guo, H. S., Cheng, Y., & Gao, Y. H. (2018). In situ observation of rock spalling in the deep tunnels of the China Jinping underground laboratory (2400 m depth). *Rock Mechanics and Rock Engineering, 51*(4), 1193–1213.

Funatsu, T., Hoshino, T., Sawae, H., & Shimizu, N. (2008). Numerical analysis to better understand the mechanism of the effects of ground supports and reinforcements on the stability of tunnels using the distinct element method. *Tunnelling and Underground Space Technology, 23*(5), 561–573.

Hoek, E., & Brown, E. T. (1996). Underground excavations in rock. In *Rev* (ed.,) (1). London: The Institution of Mining and Metallurgy.

Hoek, E., & Brown, E. T. (2019). The Hoek–Brown failure criterion and GSI – 2018 edition. *Journal of Rock Mechanics and Geotechnical Engineering, 11*(3), 445–463.

Huang, F., Zhu, H. H., Jiang, S. P., & Liang, B. (2017). Excavation-damaged zone around tunnel surface under different release ratios of displacement. *International Journal of Geomechanics, 17*(4), 04016094.

Itasca (2013). Dimensional Distinct Element Code Theory and Background. https://docs.itascacg.com/3dec700/flac3d/docproject/source/flac3dhome.html?node4659. Accessed 22 May 2024.

Li, L. P., Hu, J., Li, S. C., Qin, C. S., Liu, H. L., Chen, D. Y., & Wang, J. (2021). Development of a novel triaxial rock testing method based on biaxial test apparatus and its application. *Rock Mechanics and Rock Engineering, 54*, 1597–1607.

Li, M. Z., Li, S. R., Tian, Y., Fu, Y. H., Pei, Y. L., Zhu, W. D., & Ke, Y. L. (2023). A deep learning convolutional neural network and multi-layer perceptron hybrid fusion model for predicting the mechanical properties of carbon fiber. *Materials & Design, 227*, 111760.

Liu, F. Y., Ye, Z. J., & Wang, L. B. (2022). Deep transfer learning-based vehicle classification by asphalt pavement vibration. *Construction and Building Materials, 342*, 127997.

Ma, G. Y., He, Z. S., He, C., Kang, X. Y., Wang, S. M., & Xu, G. W. (2023). Time-dependent performance assessment of mountain tunnels considering the hazards associated with squeezing soft rock and nonuniform steel corrosion in RC lining structure. *Computers and Geotechnics, 164*, 105808.

Mou, L. T., Chang, J. L., Zhou, C., Zhao, Y. Y., Ma, N., Yin, B. C., Jain, R., & Gao, W. (2023). Multimodal driver distraction detection using dual-channel network of CNN and Transformer. *Expert Systems with Applications, 234*, 121066.

National Railway Administration of People's Republic of China (2017). *TB 10003—2016: Code for Design of Rail way Tunnel*. Beijing, China: China Railway Publishing House (in Chinese).

Nguyen, V. M., & Nguyen, Q. P. (2015). Analytical solution for estimating the stand-up time of the rock mass surrounding tunnel. *Tunnelling and Underground Space Technology, 47*, 10–15.

Nie, W., Zhao, Z. Y., Goh, A. T. C., Song, M. K., Guo, W., & Zhu, X. (2018). Performance based support design for horseshoe-shaped rock caverns using 2D numerical analysis. *Engineering Geology, 245*, 266–279.

Oke, J., Vlachopoulos, N., & Diederichs, M. S. (2014). Numerical analyses in the design of umbrella arch systems. *Journal of Rock Mechanics and Geotechnical Engineering, 6*(6), 546–564.

Packulak, T. R. M., Day, J. J., Ahmed Labeid, M. T., & Diederichs, M. S. (2022). New data processing protocols to isolate fracture deformations to measure normal and shear joint stiffness. *Rock Mechanics and Rock Engineering, 55*, 2631–2650.

Perras, M. A., & Diederichs, M. S. (2016). Predicting excavation damage zone depths in brittle rocks. *Journal of Rock Mechanics and Geotechnical Engineering, 8*(1), 60–74.

Shen, J. Y., Shu, Z., Cai, M., & Du, S. G. (2020). A shear strength model for anisotropic blocky rock masses with persistent joints. *International Journal of Rock Mechanics and Mining Sciences, 134*, 104430.

Sonmez, H., Gokceoglu, C., & Ulusay, R. (2003). An application of fuzzy sets to the Geological Strength Index (GSI) system used in rock engineering. *Engineering Applications of Artificial Intelligence, 16*(3), 251–269.

Stavrou, A., & Murphy, W. (2018). Quantifying the effects of scale and heterogeneity on the confined strength of micro-defected rocks. *International Journal of Rock Mechanics and Mining Sciences, 102*, 131–143.

Sun, B. (2021). A combined discrete element-finite difference model for simulation of double shield TBM excavation in jointed rocks. *Rock Mechanics and Rock Engineering, 54*, 5867–5883.

Sun, Q. H., Ma, F. S., Guo, J., Zhao, H. J., Li, G., Liu, S. Q., & Duan, X. L. (2021). Excavation-induced deformation and damage evolution of deep tunnels based on a realistic stress path. *Computers and Geotechnics, 129*, 103843.

Tan, X., Feng, L. J., Hu, Z. B., & Zhao, M. H. (2020). A DEM-FDM coupled numerical study on the deformation and failure process of the isolated stone column in soft soil. *Bulletin of Engineering Geology and the Environment, 79*, 1693–1705.

Wajid, M. A., Zafar, A., Terashima-Marín, H., & Wajid, M. S. (2023). Neutrosophic-CNN-based image and text fusion for multimodal classification. *Journal of Intelligent & Fuzzy Systems, 45* (1), 1039–1055.

Wang, J., Apel, D. B., Wei, C., & Xu, H. W. (2024). Prediction of strainburst risks based on the stiffness theory: Development and verification of a new rockburst indicator. *International Journal of Rock Mechanics and Mining Sciences, 175*, 105667.

Wang, M. Z., & Cai, M. (2022). Numerical modeling of stand-up time of tunnels considering time-dependent deformation of jointed rock masses. *Rock Mechanics and Rock Engineering, 55*, 4305–4328.

Yasitli, N. E. (2013). Numerical modeling of surface settlements at the transition zone excavated by New Austrian Tunneling Method and Umbrella Arch Method in weak rock. *Arabian Journal of Geosciences, 6*, 2699–2708.

Yu, W., Wang, B., Zi, X., Guo, X. X., & Wang, Z. Y. (2023). Effect of prestressed anchorage system on mechanical behavior of squeezed soft rock in large-deformation tunnel. *Tunnelling and Underground Space Technology, 131*, 104782.

Zhao, J. J. (2015). *Equivalent simulation and parameters research of the advanced small pipe grouting method*. [Master's Thesis, South China University of Technology, China] (in Chinese).

Zhao, X. B., Zhao, J., Hefny, A. M., & Cai, J. G. (2006). Normal transmission of S-wave across parallel fractures with coulomb slip behavior. *Journal of Engineering Mechanics, 132*(6), 641–650.

Zhang, Z. H., Zhu, J. B., & Deng, J. H. (2023). A comparative study for determining rock joint normal stiffness with destructive uniaxial compression and nondestructive ultrasonic wave testing. *Journal of Rock Mechanics and Geotechnical Engineering, 15*(7), 1700–1712.